

Stability and accuracy control of $\mathbf{k}\cdot\mathbf{p}$ parameters

Carlos M. O. Bastos,¹ Fernando P. Sabino,¹ Paulo E. Faria Junior,^{1,2}
Tiago Campos,¹ Juarez L. F. Da Silva,³ and Guilherme M. Sipahi^{1,2}

¹*São Carlos Institute of Physics, University of São Paulo,
PO Box 369, 13560-970, São Carlos, SP, Brazil.*

²*Department of Physics, State University of New York at Buffalo, 14260, Buffalo, New York, USA.*

³*São Carlos Institute of Chemistry, University of São Paulo,
PO Box 780, 13560-970, São Carlos, SP, Brazil.*

The $\mathbf{k}\cdot\mathbf{p}$ method is a successful approach to obtain band structure, optical and transport properties of semiconductors, and it depends on external parameters that are obtained either from experiments, tight binding or *ab initio* calculations. Despite the widespread use of the $\mathbf{k}\cdot\mathbf{p}$ method, a systematic analysis of the stability and the accuracy of its parameters is not usual in the literature. In this work, we report a theoretical framework to determine the $\mathbf{k}\cdot\mathbf{p}$ parameters from state-of-the-art hybrid density functional theory including spin-orbit coupling, providing a calculation where the gap and spin-orbit energy splitting are in agreement with the experimental values. The accuracy of the set of parameters is enhanced by fitting over several directions at once, minimizing the overall deviation from the original data. This strategy allows us to systematically evaluate the stability, preserving the accuracy of the parameters, providing a tool to determine optimal parameters for specific ranges around the Γ -point. To prove our concept, we investigate the zinc blende GaAs that shows results in excellent agreement with the most reliable data in the literature.

I. INTRODUCTION

A deep knowledge of the band structure (electronic states) of semiconductors is one of the first steps towards the understanding of a wide range of physical systems and phenomena, such as topological insulators [1–3], Majorana fermions [4–7] and polytypic nanowhiskers [8, 9] or technologies such as spintronics [10, 11]. The band structure of a given material of interest can be obtained using experimental information [12, 13] or based on theoretical calculations using different level of approximations developed along the years [14], i.e., the effects of particular interactions can be studied in details. For example, the role of the spin-orbit coupling (SOC) can be studied in detail using different approximations, which is crucial as SOC plays a critical role in the systems mentioned above.

The theoretical approaches to calculate the band structure for a given material can be separated in two lines, namely, (i) first-principles methods based on density functional theory (DFT) [15, 16] or quantum-chemistry methods such as the Hartree-Fock; (ii) phenomenological approaches such as the $\mathbf{k}\cdot\mathbf{p}$ [17, 18] or tight-binding [19–21] methods. For crystalline materials, both first-principles and phenomenological approaches can be applied and their results can be compared with experiments, and hence, their accuracy can be established. However, the use of first-principles methods for modelling confined systems such as quantum-dots, nanowires, etc, requires supercells with thousand or even million atoms, which are forbidden because of its computational cost. In contrast, the $\mathbf{k}\cdot\mathbf{p}$ method has a lower computational cost because the interactions between the particles are described by an effective potential set up by a set of parameters. The determination of such parameters is of seminal importance.

The $\mathbf{k}\cdot\mathbf{p}$ Hamiltonian is constructed using the frame-

work of perturbation theory [22, 23] and group theory analysis to reduce the number of matrix elements that are replaced by effective parameters. The number of parameters depend on the number of selected bands and on the symmetry of the described crystal. In zinc blende crystals, there is a relation allowing to calculate the effective mass parameters using the effective masses themselves [24], but for wurtzite crystal symmetry this is no longer true [25].

The effective masses can be determined experimentally using, for example, cyclotron resonance [26, 27], Hall effect [28] or optical measurements [29, 30], or theoretically, fitting a parabolic dispersion very close to Γ -point of *ab initio* band structure calculations [31, 32]. These procedures are only able to produce the effective mass parameters, leaving to other techniques the task of setting the values for the interband coupling parameters, such as the well known Kane parameter, P . This parameter is usually extracted from the effective g factor [33].

Parameters for most of the standard compounds may be found on the literature [33–36]. For example, Ref. [33] presents a compilation of parameters for almost all binary, ternary and quaternary zinc blende compounds and also for wurtzite III-nitrides, however, those parameters were obtained by mixing experimental and theoretical data, i.e., no systematic procedure was employed. The reference provides parameters for the usual 6×6 (Luttinger-Kohn [37]) and 8×8 (Kane [17] and Rashba-Sheka-Pikus [38]) band models. As we go further into the $\mathbf{k}\cdot\mathbf{p}$ models, there exist only few reliable sources of parameters for models with a higher number of bands, e.g., for 14×14 [39, 40], 20×20 [41], 24×24 [42], 34×34 [43] and 40×40 [44] bands.

In this paper, we developed a new framework to determine the $\mathbf{k}\cdot\mathbf{p}$ parameters from preexistent band structures that works with any crystal symmetry. Fitting a

set of functions derived from the secular equation of the $\mathbf{k}\cdot\mathbf{p}$ Hamiltonian to a preexistent band structure we were able to extract all the $\mathbf{k}\cdot\mathbf{p}$ parameters at once, including the interband coupling parameters. Furthermore, we performed the fitting using several different directions of the first Brillouin zone (FBZ), thus finding all the parameters in a consistent way. As a proof of concept we use a zinc blende GaAs band structure obtained by the hybrid DFT calculation with the Heyd-Scuseria-Ernzerhof functional (HSE). Since GaAs is the most studied material it will be easy to compare our results with the reported values in the literature. Furthermore, using our method we are able to predict the best set of parameters for a specific region of the FBZ. We show that, in the GaAs case, our parameters are in good agreement with the literature. We also address the accuracy of the Kane model by defining an strategy to evaluate its limits of validity. In conclusion, our method is neither limited to the crystal phase nor the Hamiltonian and opens up the possibility to study novel semiconductor systems.

The paper is organized as follows: In section II we present the the 8×8 $\mathbf{k}\cdot\mathbf{p}$ Hamiltonian. The process to

obtain DFT-HSE band structure for GaAs is shown in section III. In section IV we show the developed method for a general Hamiltonian specify the expressions for the 8×8 Hamiltonian. The application of the method to zinc blende GaAs band structure is presented in V. We proceed to the analysis of optimal parameters in section VI, comparing our results with the literature in section VII. Finally, our conclusions are shown in section VIII.

II. THE $\mathbf{k}\cdot\mathbf{p}$ METHOD

In this paper, we employed the 8×8 $\mathbf{k}\cdot\mathbf{p}$ Hamiltonian proposed by Kane [17], that extends the 6×6 Hamiltonian proposed by Luttinger-Kohn [37], in which the first-order contribution of the \mathbf{k} -dependent spin-orbit term and also the second order contribution of $\mathbf{k}\cdot\mathbf{p}$ between conduction (CB) and valence (VB) bands are neglected. Further details on the $\mathbf{k}\cdot\mathbf{p}$ Hamiltonian are discussed in the Supplemental Material. The 8×8 Kane Hamiltonian shows as

$$\begin{pmatrix} Q & S & R & 0 & i\frac{S}{\sqrt{2}} & -i\sqrt{2}R & -iP_- & 0 \\ S^\dagger & T & 0 & R & i\frac{(T-Q)}{\sqrt{2}} & i\sqrt{\frac{2}{3}}S & \sqrt{\frac{2}{3}}P_z & -\frac{1}{\sqrt{3}}P_- \\ R^\dagger & 0 & T & -S & -i\sqrt{\frac{3}{2}}S^\dagger & i\frac{(T-Q)}{\sqrt{2}} & -\frac{i}{\sqrt{3}}P_+ & -i\sqrt{\frac{2}{3}}P_z \\ 0 & R^\dagger & -S^\dagger & Q & -i\sqrt{2}R^\dagger & -i\frac{S^\dagger}{\sqrt{2}} & 0 & -P_+ \\ -i\frac{S^\dagger}{\sqrt{2}} & -i\frac{(T-Q)^\dagger}{\sqrt{2}} & i\sqrt{\frac{3}{2}}S & i\sqrt{2}R & \frac{Q+T}{2} + \Delta_{so} & 0 & -\frac{i}{\sqrt{3}}P_z & -i\sqrt{\frac{2}{3}}P_- \\ i\sqrt{2}R^\dagger & -i\sqrt{\frac{3}{2}}S^\dagger & -i\frac{(T-Q)^\dagger}{\sqrt{2}} & i\frac{S}{\sqrt{2}} & 0 & \frac{Q+T}{2} + \Delta_{so} & \sqrt{\frac{2}{3}}P_+ & -\frac{1}{\sqrt{3}}P_z \\ -iP_- & \sqrt{\frac{2}{3}}P_z & \frac{i}{\sqrt{3}}P_- & 0 & \frac{i}{\sqrt{3}}P_z & \sqrt{\frac{2}{3}}P_- & E_c & 0 \\ 0 & -\frac{1}{\sqrt{3}}P_+ & i\sqrt{\frac{2}{3}}P_z & -P_- & i\sqrt{\frac{2}{3}}P_+ & -\frac{1}{\sqrt{3}}P_z & 0 & E_c \end{pmatrix}, \quad (1)$$

where the terms are given by

$$\begin{aligned} Q &= -\frac{\hbar^2}{2m_0} [(\tilde{\gamma}_1 + \tilde{\gamma}_2)(k_x^2 + k_y^2) - (\tilde{\gamma}_1 - 2\tilde{\gamma}_2)k_z^2] & R &= -\frac{\hbar^2}{2m_0}\sqrt{3} [\tilde{\gamma}_2(k_x^2 - k_y^2) + 2i\tilde{\gamma}_3k_xk_y] \\ E_c &= E_g + \frac{\hbar^2}{2m_0}\tilde{e}k^2 & P_z &= Pk_z \\ T &= -\frac{\hbar^2}{2m_0} [(\tilde{\gamma}_1 - \tilde{\gamma}_2)(k_x^2 + k_y^2) + (\tilde{\gamma}_1 + 2\tilde{\gamma}_2)k_z^2] & S &= i\frac{\hbar^2}{2m_0} [2\sqrt{3}\tilde{\gamma}_3k_z(k_x - ik_y)] \\ P_\pm &= \frac{1}{\sqrt{2}}P(k_x \pm ik_y) & k^2 &= k_x^2 + k_y^2 + k_z^2 \end{aligned} \quad (2)$$

with the following parameters:

- $\tilde{\gamma}_1, \tilde{\gamma}_2, \tilde{\gamma}_3, \tilde{e}$: second order effective mass parameters of VB and CB. These parameters are adimensional [45].
- P : first order interaction term between states in the conduction and the valence bands. An energy

equivalent, $E_P = 2m_0P^2/\hbar^2$, may be used to analyze the effects of this parameter.

- Δ_{so} : first order SOC interaction term (energy difference between HH/LH and SO bands at Γ -point).
- E_g : energy band gap between the CB and HH/LH

bands at the Γ -point.

The Kane Hamiltonian basis set is composed by the topmost six states of VB and the first two states of CB, in the following order: $|\text{HH } \uparrow\rangle$, $|\text{LH } \uparrow\rangle$, $|\text{LH } \downarrow\rangle$, $|\text{HH } \downarrow\rangle$, $|\text{SO } \uparrow\rangle$, $|\text{SO } \downarrow\rangle$, $|\text{CB } \uparrow\rangle$, $|\text{CB } \downarrow\rangle$. HH, LH, SO and CB stand for the heavy hole, light hole, split-off hole and conduction band states, respectively. \uparrow and \downarrow are used to distinguish the total angular momentum projections. The states description using the original atomic orbital basis is given by:

$$\begin{aligned}
 |\text{HH } \uparrow\rangle &= \frac{1}{\sqrt{2}} |(X + iY) \uparrow\rangle \\
 |\text{HH } \downarrow\rangle &= \frac{i}{\sqrt{2}} |(X - iY) \downarrow\rangle \\
 |\text{LH } \uparrow\rangle &= \frac{i}{\sqrt{6}} |(X + iY) \downarrow - 2Z \uparrow\rangle \\
 |\text{LH } \downarrow\rangle &= \frac{1}{\sqrt{6}} |(X - iY) \uparrow + 2Z \downarrow\rangle \\
 |\text{SO } \uparrow\rangle &= \frac{1}{\sqrt{3}} |(X + iY) \downarrow + Z \uparrow\rangle \\
 |\text{SO } \downarrow\rangle &= \frac{i}{\sqrt{3}} |-(X - iY) \uparrow + Z \downarrow\rangle \\
 |\text{CB } \uparrow\rangle &= |S \uparrow\rangle \\
 |\text{CB } \downarrow\rangle &= |S \downarrow\rangle
 \end{aligned} \tag{3}$$

where $|X\rangle$, $|Y\rangle$ and $|Z\rangle$ are the p-type like states (p_x , p_y and p_z) and $|S\rangle$ the s-like ones and \uparrow and \downarrow represent their spins.

III. GaAs HYBRID DFT-HSE BAND STRUCTURE

The *ab initio* GaAs band structure was obtained through the use of hybrid DFT calculations within the HSE [46] exchange-correlation (XC) functional where the energy is given by the following equation,

$$E_{\text{xc}}^{\text{HSE}} = \alpha E_{\text{x}}^{\text{SR}}(\mu) + (1 - \alpha) E_{\text{x}}^{\text{PBE,SR}} + E_{\text{x}}^{\text{PBE,LR}} + E_{\text{c}}^{\text{PBE}}. \tag{4}$$

In the HSE formulation, the exchange energy is partitioned into two terms, namely, short range (SR) and long range (LR) terms. A screening nonlocal Fock operator is employed to obtain the SR term, in which the μ parameter ($\mu = 0.206 \text{ \AA}^{-1}$) determines the intensity of the screening [47], while the LR term is described by the semilocal Perdew-Burke-Ernzerhof (PBE) [48] functional. The parameter α defines the percentage of the nonlocal SR exchange term, and it is 0.25 in the HSE06 functional. However, this particular value was obtained for typical molecules, based on the analysis of the adiabatic connection formula and the lowest order of Görling-Levy perturbation theory [48], and consequently does not yield a correct band gap (although better than PBE) for most of the materials [47–49]. Therefore, the α parameter can be assumed as a fitting parameter, which can be adjusted to reproduce particular bulk properties, e.g.,

energy band gap, lattice parameter, etc. We have fitted α to yield the fundamental experimental GaAs band gap [23, 33] (i.e., 1.519 eV).

To solve the Kohn-Sham equation, we employed the projected augmented wave (PAW) method [50, 51], as implemented in Vienna *Ab-initio* Simulation Package (VASP) [52, 53], and the PAW projectors provided within VASP to describe the following valence states, $4s^2 4p^3$ for As and $3d^{10} 4s^2 4p^1$ for Ga. To describe the valence electronic states, we employed the scalar relativistic approximation, in which the SOC effects for the valence states were taken into account by perturbation theory employing 38 empty states. For the total energy and band structure calculations, we employed a cutoff energy of 455 eV, while a cutoff energy of 607 eV was used to obtain the equilibrium volume by the minimization of the stress tensor. For the Brillouin zone integration, we employed a \mathbf{k} -point mesh of $8 \times 8 \times 8$, which yields accurate results.

GaAs crystallize in the well known zinc blende structure with space group T_d and one formula unit per primitive unit cell, in which every Ga atom is surrounded by four As atoms (tetrahedral symmetry), and vice-versa. Using the fact that the band gap of a semiconductor increases almost linearly by increasing the percentage of the α (nonlocal Fock term) parameter [49] we set $\alpha = 0.317$, finding a GaAs band gap of 1.521 eV, which deviates by 14 % from the experimental result. We obtained an equilibrium lattice parameter of 5.652 \AA , which deviates by 1 % compared with the experimental results. However, we would like to point out that using $\alpha = 0$ yields $a_0 = 5.733 \text{ \AA}$. Furthermore, total calculations at the same lattice constant without the SOC for the valence states increase the band gap to 1.627 eV.

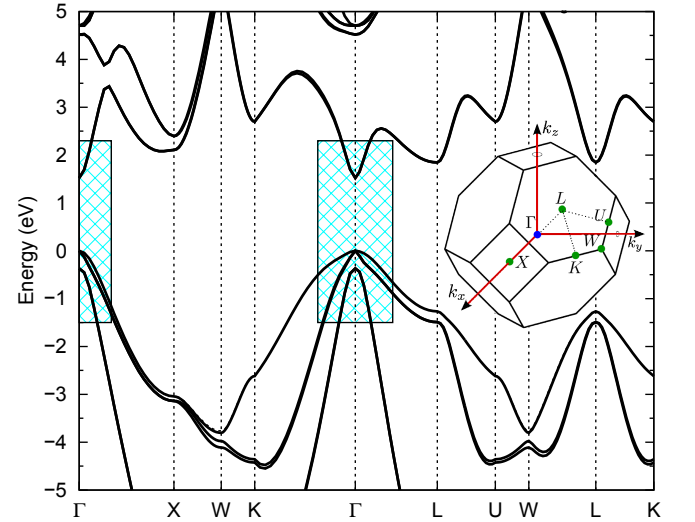


FIG. 1. Band structure for GaAs zinc blende with the respective FBZ and the high symmetry points. The highlighted regions indicate the approximate region where Kane Hamiltonian is valid.

Fig. 1 presents the band structure with SOC for the valence states on the usual high-symmetry Brillouin lines. Both the VBM and the CBM are located at the Γ -point, as expected [33]. In the absence of SOC (not shown here), the highest valence band is composed by a sixfold degenerate state (each band being twofold degenerate in spin) at Γ -point. However, when the SOC is considered this degeneracy is broken in a twofold degenerate, split-off band, and a fourfold degenerate band that still remains the highest valence band. The energy difference between these states are $\Delta_{so} = 0.369$ eV which is 8 % bigger than the experimental value, 0.341 eV [33]. Even though the band gap was fitted to yield the experimental result, the Δ_{so} parameter was not fitted in our calculations, which explains this difference. For \mathbf{k} -points other than Γ , SOC still breaks the degeneracy of the highest valence band, creating the heavy and light holes bands. A closer look will show that in less symmetric points, e. g. along the $\Gamma - K$ line, the degeneracy is further broken, creating bands with no degeneracy. The present results are consistent with the literature, including SOC or not.

To ensure high quality data for the fitting along the desired $\Gamma - X$, $\Gamma - L$ and $\Gamma - K$ lines, we calculated a large number of \mathbf{k} -points along each line. Because of the perturbation theory used in the $\mathbf{k}\cdot\mathbf{p}$ method, we expect to fit the parameters only at a defined region around the Γ -point. In order to reduce the high computational cost of the hybrid DFT-HSE+SOC approach, we restricted \mathbf{k} -points to 100 samples up to 50 % of the FBZ.

IV. THE FITTING METHOD

Along the years, $\mathbf{k}\cdot\mathbf{p}$ parameters are usually being derived from effective masses using experimental data [36, 54–57] or from theoretical band structure calculations [32, 58–63]. Although this procedure is relatively simple, it is not always possible to find analytical solutions relating $\mathbf{k}\cdot\mathbf{p}$ parameters to the effective masses. Alternatively, the determination of the parameters may rely on the fitting of previously calculated band structures [31, 60, 64–69]. However, details about the fitting approach are not usually described by the authors.

Although we consider a fitting that is based on the resolution of the secular equation, as in previous works [59, 68, 70], we used it in a different way. The secular equation is used to reduce the complexity of the fitting. Using the property that the eigenvalues are roots of the secular equation and, by consequence, assuming that we can collect expressions for any of the coefficients that must also be zero, we extract a new set of n equations (n being the order of the original matrix) that are used in our fitting. With this procedure, we make explicit the couplings among the different bands, simplifying the expressions to be solved. The functions determined for each direction are used together to provide the fitting that minimizes the euclidean distance of the full set of equations to the previously calculated data at once. Be-

cause we determine all the distances in a single step, we guarantee that no direction is assigned more importance than any other. In fact, the addition of other directions to the fitting provides a way to increase the accuracy.

The general form of any $\mathbf{k}\cdot\mathbf{p}$ matrix with n energy bands is given by

$$\begin{pmatrix} \alpha_{11}(\mathbf{k}, \{p\}) & \dots & \alpha_{1i}(\mathbf{k}, \{p\}) & \dots & \alpha_{1n}(\mathbf{k}, \{p\}) \\ \vdots & & \ddots & & \vdots \\ \alpha_{i1}^\dagger(\mathbf{k}, \{p\}) & \dots & \alpha_{ii}(\mathbf{k}, \{p\}) & \dots & \alpha_{in}(\mathbf{k}, \{p\}) \\ \vdots & & \ddots & & \vdots \\ \alpha_{1n}^\dagger(\mathbf{k}, \{p\}) & \dots & \alpha_{in}^\dagger(\mathbf{k}, \{p\}) & \dots & \alpha_{nn}(\mathbf{k}, \{p\}) \end{pmatrix}, \quad (5)$$

where the matrix elements, $\alpha_{ij}(\mathbf{k}, \{p\})$ are functions that represent each matrix element with \mathbf{k} being the wave vector and $\{p\}$, the set of $\mathbf{k}\cdot\mathbf{p}$ parameters to be determined.

The secular equation of the Hamiltonian (5) may be written as a general polynomial for the eigenvalues ϵ

$$\begin{aligned} & c_{n-1}(\alpha_{11}(\mathbf{k}, \{p\}), \dots, \alpha_{nn}(\mathbf{k}, \{p\})) \epsilon^{n-1}(\mathbf{k}) \\ & + \dots + c_1(\alpha_{11}(\mathbf{k}, \{p\}), \dots, \alpha_{nn}(\mathbf{k}, \{p\})) \epsilon(\mathbf{k}) \\ & + c_0(\alpha_{11}(\mathbf{k}, \{p\}), \dots, \alpha_{nn}(\mathbf{k}, \{p\})) = -\epsilon^n(\mathbf{k}), \end{aligned} \quad (6)$$

where c_i are the polynomial coefficients, functions of the matrix elements $\alpha_{ij}(\mathbf{k}, \{p\})$. Since these coefficients are functions of \mathbf{k} and $\{p\}$, we can denote them as $c_i(\mathbf{k}, \{p\})$, rewriting the above equation as

$$\sum_{i=0}^{n-1} c_i(\mathbf{k}, \{p\}) \epsilon^i(\mathbf{k}) = -\epsilon^n(\mathbf{k}). \quad (7)$$

The analytical forms of these coefficients are used as the fitting functions on our approach, and will be identified as *analytical functions*, denoted by the super-index A :

$$\begin{cases} c_0^A(\mathbf{k}, \{p\}) \\ c_1^A(\mathbf{k}, \{p\}) \\ \vdots \\ c_{n-1}^A(\mathbf{k}, \{p\}) \end{cases}. \quad (8)$$

The next step is to find a similar relation for the eigenvalues obtained from the preexistent band structures, from now on called *reference band structure*. Assuming that the eigenvalues satisfy the secular equation, we can write a system of equations to determine the polynomial coefficients as a function of the wave vector \mathbf{k} :

$$\begin{pmatrix} 1 & \epsilon_1(\mathbf{k}) & \dots & \epsilon_1^i(\mathbf{k}) & \dots & \epsilon_1^{n-1}(\mathbf{k}) \\ \vdots & \vdots & \ddots & \vdots & \ddots & \vdots \\ 1 & \epsilon_i(\mathbf{k}) & \dots & \epsilon_i^i(\mathbf{k}) & \dots & \epsilon_i^{n-1}(\mathbf{k}) \\ \vdots & \vdots & \ddots & \vdots & \ddots & \vdots \\ 1 & \epsilon_n(\mathbf{k}) & \dots & \epsilon_n^i(\mathbf{k}) & \dots & \epsilon_n^{n-1}(\mathbf{k}) \end{pmatrix} \begin{pmatrix} c_0(\mathbf{k}) \\ c_1(\mathbf{k}) \\ \vdots \\ c_i(\mathbf{k}) \\ \vdots \\ c_{n-1}(\mathbf{k}) \end{pmatrix} = - \begin{pmatrix} \epsilon_1^n(\mathbf{k}) \\ \vdots \\ \epsilon_i^n(\mathbf{k}) \\ \vdots \\ \epsilon_n^n(\mathbf{k}) \end{pmatrix}, \quad (9)$$

where $\epsilon_i(\mathbf{k})$ represents the i -th energy band.

Therefore, using eigenvalues from the *reference band structure*, we can solve this system to obtain the coefficients c_i as functions of $\epsilon_i(\mathbf{k})$. This form of the coefficients will be called *numerical functions*, denoted by the super-index N :

$$\begin{cases} c_0^N[\epsilon_1(\mathbf{k}), \epsilon_2(\mathbf{k}), \dots, \epsilon_n(\mathbf{k})] \\ c_1^N[\epsilon_1(\mathbf{k}), \epsilon_2(\mathbf{k}), \dots, \epsilon_n(\mathbf{k})] \\ \vdots \\ c_{n-1}^N[\epsilon_1(\mathbf{k}), \epsilon_2(\mathbf{k}), \dots, \epsilon_n(\mathbf{k})] \end{cases} \quad (10)$$

Since we want to use the $\mathbf{k}\cdot\mathbf{p}$ to describe our *reference band structure*, we should now consider that both numerical and analytical forms of the coefficients are equivalent, leading to the equality

$$\begin{cases} c_0^A(\mathbf{k}, \{p\}) = c_0^N[\epsilon_1(\mathbf{k}), \epsilon_2(\mathbf{k}), \dots, \epsilon_n(\mathbf{k})] \\ c_1^A(\mathbf{k}, \{p\}) = c_1^N[\epsilon_1(\mathbf{k}), \epsilon_2(\mathbf{k}), \dots, \epsilon_n(\mathbf{k})] \\ \vdots \\ c_{n-1}^A(\mathbf{k}, \{p\}) = c_{n-1}^N[\epsilon_1(\mathbf{k}), \epsilon_2(\mathbf{k}), \dots, \epsilon_n(\mathbf{k})] \end{cases} \quad (11)$$

Having both, analytical and numerical functions, we can perform the fitting procedure to extract the $\mathbf{k}\cdot\mathbf{p}$ parameters that best describe the *reference band structure*. The fitting was done using the nonlinear least squares method, implemented on MathematicaTM using the Non-LinearModelFit routine [71]. Several different minimization methods were tested: Newton, QuasiNewton, LevenbergMarquardt, Gradient, Conjugate Gradient. As the results were similar for all tested methods, we chose the Conjugate Gradient method due to its relatively low memory requirements for a large-scale problem and simplicity of its iteration [72].

The fitting method described above is general, and it can be applied for any given system, even for $\mathbf{k}\cdot\mathbf{p}$ Hamiltonians larger than 8×8 and any direction in the FBZ. For the particular case of semiconductors with zinc blende structures, we can sample the FBZ along the three most relevant high-symmetry directions, namely, $\Gamma - X$, $\Gamma - K$, and $\Gamma - L$. The number of \mathbf{k} -point lines play an important role, e.g., the direction $\Gamma - L$ can yield only the $\tilde{\gamma}_1$ and $\tilde{\gamma}_3$ parameters, and hence, additional directions are required to identify the $\tilde{\gamma}_2$ parameter.

For the case of the Hamiltonian given in eq. (1), the secular equation can always be factorized in the separate components, reducing the dimension of the problem by half. The factorized secular equation reads as

$$\begin{aligned} [c_0^N(\mathbf{k}, \{p\}) + c_1^N(\mathbf{k}, \{p\})\epsilon + c_2^N(\mathbf{k}, \{p\})\epsilon^2 \\ + c_3^N(\mathbf{k}, \{p\})\epsilon^3 + \epsilon^4]^2 = 0, \end{aligned} \quad (12)$$

where $\{p\} = \{\tilde{\gamma}_1, \tilde{\gamma}_2, \tilde{\gamma}_3, \Delta_{so}, P, E_g, \tilde{e}\}$. In specific directions the secular equation may be further factorized.

Solving the system (12), we obtain the following relations for the numerical coefficients

$$\begin{aligned} c_{HH}^N(k_{\Gamma X}) &= -\epsilon_{HH}(k_{\Gamma X}), \\ c_2^N(k_{\Gamma X}) &= -\epsilon_{CB}(k_{\Gamma X}) - \epsilon_{LH}(k_{\Gamma X}) - \epsilon_{SO}(k_{\Gamma X}), \\ c_1^N(k_{\Gamma X}) &= \epsilon_{CB}(k_{\Gamma X})\epsilon_{LH}(k_{\Gamma X}) + \epsilon_{CB}(k_{\Gamma X})\epsilon_{SO}(k_{\Gamma X}) \\ &\quad + \epsilon_{LH}(k_{\Gamma X})\epsilon_{SO}(k_{\Gamma X}), \\ c_0^N(k_{\Gamma X}) &= \epsilon_{CB}(k_{\Gamma X})\epsilon_{LH}(k_{\Gamma X})\epsilon_{SO}(k_{\Gamma X}). \end{aligned} \quad (13)$$

Notice that in the previous expressions, ϵ_1 , ϵ_2 , ϵ_3 and ϵ_4 where replaced by the average of the eigenvalues of the bands at the specific k -point: ϵ_{CB} , ϵ_{HH} , ϵ_{LH} and ϵ_{SO} .

The parameters Δ_{so} and E_g can be directly found from the Γ -point energies and used as input to the fitting approach. Since, we adjusted simultaneously the expressions for all the different bands in all chosen directions of the FBZ, the overall quality of the parameters for the multiband Hamiltonian is guaranteed.

V. $\mathbf{k}\cdot\mathbf{p}$ PARAMETERS FOR ZINC BLENDE GaAs

In Fig. 2, we show the results of the fitting, using 20 % of the FBZ superposed to the original DFT-HSE+SOC calculation. For this particular range, we have found the following set of parameters: $\gamma_1 = 1.31$, $\gamma_2 = -0.72$, $\gamma_3 = 0.03$ and $e = -2.50$ in units of $\hbar^2/2m_0$; $P = 9.75$ eV Å. A first inspection shows that the most important features of the band structure are preserved. The band structure for this range of wave vectors has essentially two different regions, one up to 8 % of the FBZ and a second from 8 % to 20 %. The HH and LH bands present nearly parabolic behavior in both regions, but the effective masses if calculated only inside each region, would be clearly different. The non-parabolicity, or band scattering, around 8 % and the quasi linear behavior of the conduction band and the split-off hole bands after the non-parabolicity are in good agreement with the *reference band structure*. Finally, a simple visual inspection of this results shows that the difference between the curves is smaller than 8 % at the borders of the region.

To avoid using visual estimation of the agreement of curves, it is necessary to find a procedure that numerically determines how close the DFT-HSE+SOC and the 8×8 $\mathbf{k}\cdot\mathbf{p}$ band structures are with respect to each other. This analysis can also be used to determine if in a smaller region, an optimized parameter can lead to more reliable results. To evaluate the agreement, we performed fittings over different ranges around the Γ -point, from 2 % up to 20 % of the FBZ, obtaining a large number of $\mathbf{k}\cdot\mathbf{p}$ parameter sets.

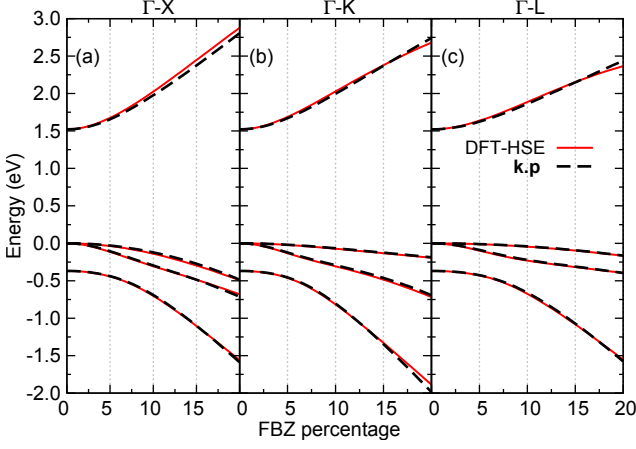


FIG. 2. Comparison between the band structure obtained by diagonalization of the $\mathbf{k}\cdot\mathbf{p}$ Hamiltonian with the 20 % region parameter set (dashed lines) and the band structure obtained by hybrid DFT-HSE+SOC (solid lines). We show three directions of the FBZ: (a) $\Gamma - X$, (b) $\Gamma - K$ and (c) $\Gamma - L$. The x-axis shows percentage in the specific direction.

VI. OPTIMAL PARAMETER SET

In order to evaluate the assertiveness of our parameters, we employed the Root Mean Square Deviation (RMSD) to compare the *reference* and *parametrized* band structures using the appropriate definition of the RMSD to our problem

$$\text{RMSD} = \sqrt{\frac{1}{N} \sum_d \sum_{\mathbf{k}_d} \sum_n [\epsilon_n^p(\mathbf{k}_d) - \epsilon_n^r(\mathbf{k}_d)]^2} \quad (14)$$

where the summations run over the directions in which the FBZ was sampled, d , the points of the reciprocal space calculated in each direction, \mathbf{k}_d , and the bands taken into account, n . N_d , $N_{\mathbf{k}}$ and N_n are the total values of each one of these variables. The super-index p (r) in the energy bands denotes the *parametrized* (*reference*) band structure. Notice that the normalization condition (with $N = N_d \times N_{\mathbf{k}} \times N_n$) allows us to compare sets with different numbers of points. The smaller the value of the RMSD, the better our Hamiltonian and parameters fit the DFT-HSE+SOC band structure.

The search for the optimal parameter set is performed as follows: (i) we determine the parameter sets for different fitting percentages of the FBZ; (ii) for each of these parameter sets, we calculate the RMSD for different FBZ percentages; (iii) the optimal parameter set presents the minimum RMSD value for a given FBZ percentage. We considered 16 different percentage values in the range from 2 % to 20 %, that were used to define either the parameter sets and the analyzed region.

In Fig. 3(a) we show the RMSD density map, with y -axis representing the fitting percentage of the parameter sets and the x -axis, the FBZ percentage used in the

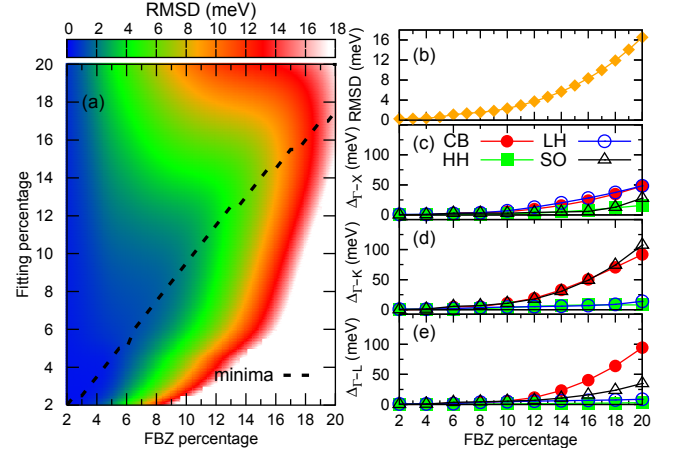


FIG. 3. (a) Root mean square deviation (RMSD) density map showing the agreement of the different adjusted parameter sets against the range around the Γ -point they are sampled. The optimal parameter sets are indicated by the dashed line. (b) RMSD of the optimal set of parameters for each enclosing region. (c), (d) and (e) show the maximum deviation for each optimal parameter set for the three directions used in the fitting process.

RMSD determination. The lowest RMSD values for each range are represented by the black dashed line. These parameter sets represent the best parameters that describe each range. We found that all parameter sets reproduce the band structure in the region below 6 % with an average deviation of around 2 meV. If the parameter set is in the fitting range between 6 % and 14 %, the region of optimal agreement is extended to approximately 12 % of the FBZ with just a slight increase of the RMSD value. If one considers a higher deviation, e.g. 10 meV, this region would be extended to around 15 %. Animations of the optimal $\mathbf{k}\cdot\mathbf{p}$ band structure changes with the fitting region limit can be found in the Supplemental Materials.

Fig. 3(b) shows the RMSD for the optimal parameters sets. We can see an increase of the average deviation by the increase of the FBZ range. This would be expected since the 8×8 $\mathbf{k}\cdot\mathbf{p}$ Hamiltonian is valid in a region around Γ -point. The results presented here show that the average deviation for the 20 % range is still below 20 meV, reasonable for most of the optical simulations and for ranges below 14 % the average deviation is only 4 meV.

The maximum deviation from the DFT-HSE calculation for each range in the 3 different directions, $\Gamma - X$, $\Gamma - K$ and $\Gamma - L$, is shown in Figs. 3(c)-(e), respectively. Although CB and SO present large deviations at 20 % of the FBZ (approx. 100 meV along $\Gamma - K$ for CB and SO and also along $\Gamma - L$ for CB), for all other sampled curves, the bands present up to this percentage a deviation much smaller (around 50 meV for CB and LH at $\Gamma - X$ and smaller than 25 meV for all others). The large values of the deviation for CB and SO, indicate that they are mainly responsible for the steep increase of the RMSD

around 15%, i.e., all other curves have a very small deviation up to this percentage.

A general overview of the parameter sets with and without the optimization approach is presented in Fig. 4 for different FBZ regions. The dashed lines represent the raw data, i.e., the parameter sets obtained directly from the fitting of the specific range while the solid lines are used for the optimal parameters for the same range. One can clearly distinguish two different regions: i) below 7%, we can see a fast decay of the values for the interband interaction parameter, P , (on top) and a fast increase for the effective masses (on bottom); and ii) above 7%, the parameters are almost stable with a very slight linear variation.

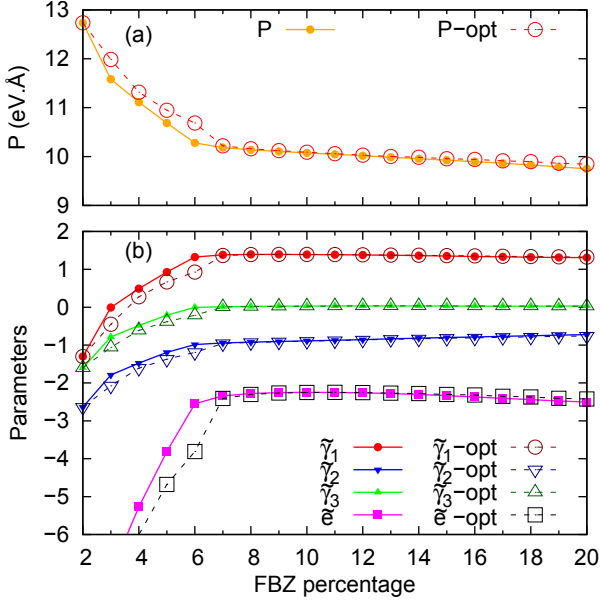


FIG. 4. Comparison between optimal and non optimal parameter sets. (a) P parameter in $\text{eV}\cdot\text{\AA}$ units and (b) $\tilde{\gamma}_1$, $\tilde{\gamma}_2$, $\tilde{\gamma}_3$ and \tilde{e} .

Analyzing the band structure behavior, it is easy to notice that using a range that takes into account the non-parabolicity around 8% is essential to determine a stable set of parameters. In light of Fig. 3(b) however, one can state that, even with the stability of the parameter values, an optimal set must be chosen to enhance the accuracy of the fitting. This can be seen on Fig. 5, where we present the agreement of *parametrized* and *reference* band structures for the optimal (solid lines) and non-optimal (dashed lines) parameter sets for the range of 20%. The optimal parameters for 20% were obtained for the fitting using the range of 17.5% and read as: $\tilde{\gamma}_1 = 1.28$, $\tilde{\gamma}_2 = -0.73$, $\tilde{\gamma}_3 = 0.03$ and $\tilde{e} = -2.34$ and $P = 9.85 \text{ eV}\cdot\text{\AA}$. Since the behavior of the bands in the different directions is very similar, we chose to present only the $\Gamma - L$ direction. The Supplemental Materials provide other directions expressions. The differences are more striking in conduction and split-off bands, where the choice of the parameters can reduce the total devi-

ation to approximately two thirds for an specific point, i. e. from 25 to 15 meV on CB and from 15 to 10 meV on SO. To see a complete table with optimal parameters for the full range of enclosing regions, please refer to the Supplemental Materials.

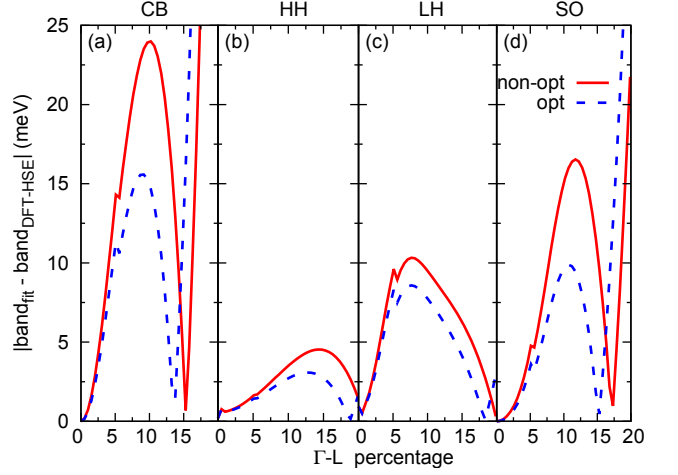


FIG. 5. Difference between the DFT-HSE and $\mathbf{k}\cdot\mathbf{p}$ band structures calculated with optimal (solid lines) and non-optimal (dashed lines) parameter sets along $\Gamma - L$ direction for: (a) CB; (b) HH; (c) LH; and (d) SO bands. The optimal parameters set shows better agreement with the DFT-HSE band structure. Other directions show similar behaviors.

VII. COMPARISON WITH LITERATURE PARAMETERS

The literature presents in general a unique set of parameters for any material. As we suggest optimal parameters for specific ranges of the FBZ, in our comparison we chose 7 different parameter sets from the literature [33, 36, 54–56, 58, 73], see table in A. Using these sets, we calculated the average value for each parameter and its standard deviation. In Fig. 6 we plot the optimal parameters together with shadowed regions showing the intervals of the standard deviation around the average values of the parameters. Our results show good agreement with the literature data in general, since the values obtained for ranges larger than 7% are stable and lie always inside the standard deviation interval around the average of the values selected from the literature.

The behavior presented for regions smaller than 7% may be understood by a simple analysis the band structure and the role of E_p in the secular equation. E_p can be adimensionalized by defining a new parameter that reads as $\tilde{\gamma}_P = E_p/E_g$, showing that, even if P appears in first order perturbation terms, $\tilde{\gamma}_P$ acts as an effective mass parameter. According to this new definition, we have now five different effective mass parameters and four bands to do the fitting. As up to 7%, the bands show a clear parabolic behavior, the fitting of the pa-

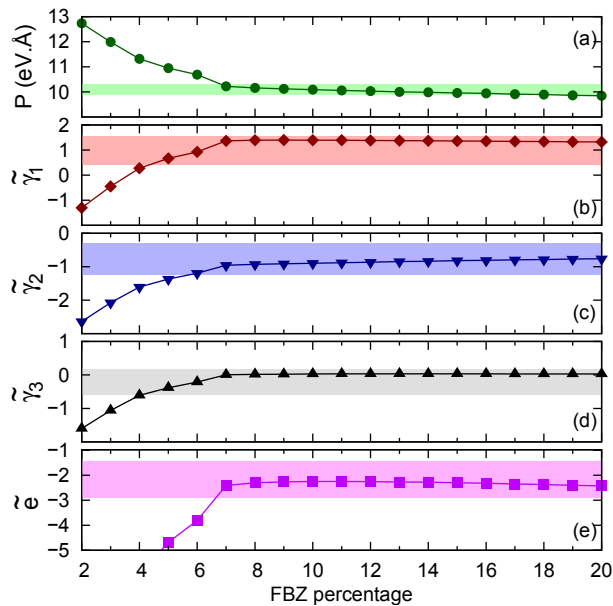


FIG. 6. Comparison of the optimal parameters with the literature. The optimal parameters are shown in the curves and the shadowed regions present the intervals of the standard deviation around the average values of the parameters, determined from 7 traditional papers. (a) P parameter in eV \AA , and (b) $\tilde{\gamma}_1$, (c) $\tilde{\gamma}_2$, (d) $\tilde{\gamma}_3$ and (e) \tilde{e} .

rameters become undetermined. Around this percentage all the bands start mixing and non-parabolic behavior may be seen. Just above this region, a new parabolic behavior emerges and all the bands change their curvatures accordingly. Including the two parabolic regions in the fitting, e. g., fitting from Γ to 12 %, provides the necessary relations to distinguish among the different parameters influence on the effective masses, giving parameters that agree with the literature parameters as can be seen in Fig. 6. An evaluation of the method can be done by analysing the exceptional agreement with literature parameters. The curvatures obtained by our fitting reproduce the most reliable data from literature. Moreover, this indicates that the choice of hybrid DFT-HSE combined methods reproduce accurately the properties of the actual electronic properties of the material, validating our choice.

Finally, joining the information of the agreement of the model with literature parameters together with the deviation from the DFT-HSE calculation described in section VI, we have a tool to assess some insights about the accuracy of the effective mass approximation. The lack of agreement of the fitting after 15 %, specially for the CB and SO bands, suggests that this specific approximation starts to lose its validity at this region. However, even in this region, our calculations indicate an average deviation of less than 15 meV, indicating that, with proper parameters, the determination of properties depending on band structures inside this range of the FBZ are reliable.

VIII. CONCLUSIONS

We developed and implemented a general method to extract multiband $\mathbf{k}\cdot\mathbf{p}$ parameters using the secular equation of the Hamiltonian. Our approach considers the simultaneous fitting of multiple directions of the FBZ of preexistent band structure and, combined with the RMSD analysis, provides a tool to evaluate the global deviation between the fitted and the original data in a systematic way. Within this approach, an optimal set of parameters may be proposed for each specific region of the FBZ.

In order to test our approach, we fitted the conventional 8×8 zinc blende Hamiltonian to GaAs band structure obtained by a state-of-the-art hybrid DFT-HSE+SOC calculation. The use of hybrid potentials provided a way of guaranteeing that the electronic properties of the systems are directly associated with their experimental values, addressing the most important issues when using DFT calculations to determine effective parameters.

Our fitted band structures present good agreement with the DFT values when using up to 20 % of FBZ. Particularly, below 15 % we showed an average deviation of less than 10 meV. Above this range, we found that the deviation rapidly increases due to the lack of additional coupling terms in the Hamiltonian. Besides the good agreement on regions below 7 %, our analysis show that the parameters are not stable in this range. The stability present above 7 % and the small deviation below 15 % define the range that can be used to obtain parameter sets that accurately describe the band structure up to 20 % of the FBZ. Finally, the comparison with experimental and theoretical available data show that the optimal parameter sets lie inside the range of the most reliable parameters from the literature.

Concluding, our approach provides a method of finding parameters for a general $\mathbf{k}\cdot\mathbf{p}$ model allowing its use for any phase or crystalline structure. As a consequence it can be used to extract parameters of new $\mathbf{k}\cdot\mathbf{p}$ Hamiltonians, opening a large range of opportunities to study new physical phenomena.

ACKNOWLEDGEMENTS

The authors acknowledge financial support from the Brazilian agencies CNPq (grant #246549/2012-2), FAPESP (grants #2011/19333-4, #2012/05618-0 and #2013/23393-8) and CAPES (PVE grant #88881.068174/2014-01).

Appendix A: Parameters table for comparison with the literature

In section VII we compared the optimal parameters for a region comprising up to 20 % with the literature.

TABLE I. $\mathbf{k}\cdot\mathbf{p}$ parameters obtained in this work (using 20 % of the FBZ) and from selected references showing well established $\mathbf{k}\cdot\mathbf{p}$ parameter sets. P is given in eV Å.

	this work	literature						
	fit (20 %)	ref.[33]	ref.[36]	ref. [58]	ref. [73]	ref. [54]	ref. [55]	ref. [56]
$\tilde{\gamma}_1$	1.28	0.66	0.36	2.02	0.60	0.98	0.47	1.21
$\tilde{\gamma}_2$	-0.73	-1.10	-1.08	-0.41	-1.17	-0.61	-1.24	-0.10
$\tilde{\gamma}_3$	0.03	0.23	-0.45	0.46	-0.37	-0.61	-0.48	-0.07
\tilde{e}	-2.34	-2.87	-3.28	-0.94	-2.18	-2.62	-2.76	-1.77
P	9.85	10.47	10.25	9.89	10.27	10.37	10.48	10.18

In table I we present the literature data used to calculate the average and standard deviation of the parameters.

- [1] Bernevig B A, Hughes T L and Zhang S C 2006 *Science* **314** 1757–1761
- [2] Baum Y, Böttcher J, Brüne C, Thienel C, Molenkamp L W, Stern A and Hankiewicz E M 2014 *Physical Review B* **89**(24) 245136
- [3] Miao M S, Yan Q, Van de Walle C G, Lou W K, Li L L and Chang K 2012 *Physical Review Letters* **109** 186803
- [4] Alicea J 2012 *Reports on Progress in Physics* **75** 076501
- [5] Mourik V, Zuo K, Frolov S M, Plissard S R, Bakkers E P A M and Kouwenhoven L P 2012 *Science* **336** 1003–1007
- [6] Stanescu T D and Tewari S 2013 *Journal of Physics: Condensed Matter* **25** 233201
- [7] Reuther J, Alicea J and Yacoby A 2013 *Physical Review X* **3**(3) 031011
- [8] Faria Junior P E and Sipahi G M 2012 *Journal of Applied Physics* **112** 103716
- [9] Faria Junior P E, Campos T and Sipahi G M 2014 *Journal of Applied Physics* **116** 193501
- [10] Jungwirth T, Wunderlich J, Novák V, Olejník K, Gallagher B L, Campion R P, Edmonds K W, Rushforth A W, Ferguson A J and Nêmec P 2014 *Reviews of Modern Physics* **86**(3) 855–896
- [11] Lazić P, Sipahi G M, Kawakami R K and Žutić I 2014 *Physical Review B* **90**(8) 085429
- [12] Kane E O 1957 *Journal of Physics and Chemistry of Solids* **1** 249–261
- [13] Walukiewicz W, Ager J W, Yu K M, Liliental-Weber Z, Wu J, Li S X, Jones R E and Denlinger J D 2006 *Journal of Physics D-applied Physics* **39** R83–R99
- [14] Jones R O 2015 *Rev. Mod. Phys.* **87** 897–923
- [15] Hohenberg P and Kohn W 1964 *Physical Review* **136** B864–B871
- [16] Kohn W and Sham L J 1965 *Physical Review* **140** A1133–A1138
- [17] Kane E 1966 (*Semiconductors and Semimetals* vol 1) ed Willardson R and Beer A C (Elsevier) pp 75 – 100
- [18] Sipahi G M, Enderlein R, Solfaro L M R, Leite J R, da Silva E C F and Levine A 1998 *Physical Review B* **57**(15) 9168–9178
- [19] Slater J C and Koster G F 1954 *Physical Review* **94**(6) 1498–1524
- [20] Harrison W 1989 Dover Books on Physics (Dover Publications)
- [21] Goringe C M, Bowler D R and Hernandez E 1997 *Reports on Progress in Physics* **60** 1447
- [22] Enderlein R and Horing J M N 1997 (Singapore: World Scientific)
- [23] Willatzen M and Lew Yan Voon L C 2009 (Berlin, Heidelberg: Springer Berlin Heidelberg)
- [24] Enderlein R, Sipahi G M, Solfaro L M R and Leite J R 1998 *physica status solidi (b)* **206** 623–633
- [25] Chuang S L and Chang C S 1996 *Physical Review B* **54**(4) 2491–2504
- [26] Mears A and Stradling R 1971 *Journal of Physics C: Solid State Physics* **4** L22
- [27] Herlach F 1974 *Journal of Physics C: Solid State Physics* **7** L308
- [28] Becker W M, Ramdas A K and Fan H Y 1961 *Journal of Applied Physics* **32** 2094–2102
- [29] Spitzer W G and Fan H Y 1957 *Physical Review* **106**(5) 882–890
- [30] Cardona M 1961 *Physical Review* **121**(3) 752–758
- [31] Dugdale D J, Brand S and Abram R A 2000 *Physical Review B* **61** 12933–12938
- [32] Ramos L E, Teles L K, Solfaro L M R, Castineira J L P, Rosa A L and Leite J R 2001 *Physical Review B* **63** 165210
- [33] Vurgaftman I, Meyer J R and Ram-Mohan L R 2001 *Journal of Applied Physics* **89** 5815
- [34] Boujdaria K, Ridene S and Fishman G 2001 *Physical Review B* **63** 235302
- [35] Vurgaftman I and Meyer J R 2003 *Journal of Applied Physics* **94** 3675
- [36] Shokhovets S, Ambacher O and Gobsch G 2007 *Physical Review B* **76** 125203
- [37] Luttinger J M and Kohn W 1955 *Physical Review* **97** 869–883
- [38] Sirenko Y M, Jeon J B, Kim K W, Littlejohn M A and Strosio M A 1996 *Physical Review B* **53**(4) 1997–2009
- [39] Jancu J M, Scholz R, de Andrada e Silva E and La Rocca G 2005 *Physical Review B* **72** 193201
- [40] Winkler R 2003 (*Springer Tracts in Modern Physics* vol 191) (Berlin, Heidelberg: Springer Berlin Heidelberg)
- [41] Radhia S B, Ridene S, Boujdaria K, Bouchriha H and Fishman G 2002 *Journal of Applied Physics* **92** 4422
- [42] Ben Radhia S, Boujdaria K, Ridene S, Bouchriha H and Fishman G 2003 *Journal of Applied Physics* **94** 5726
- [43] Saïdi I, Ben Radhia S and Boujdaria K 2008 *Journal of Applied Physics* **104** 023706
- [44] Sadi I, Ben Radhia S and Boujdaria K 2010 *Journal of Applied Physics* **107** 043701
- [45] The tilde is used, as in $\tilde{\gamma}_1$, to refer to the Kane model parameters in opposition to the Luttinger parameters, defined in Ref. [37], that are noted without it, as in γ_1 .

- [46] Heyd J, Scuseria G E and Ernzerhof M 2003 *Journal of Chemical Physics* **118** 8207–8215
- [47] Heyd J and Scuseria G E 2004 *The Journal of Chemical Physics* **121** 1187–1192
- [48] Perdew J P, Ernzerhof M and Burke K 1996 *The Journal of Chemical Physics* **105** 9982–9985
- [49] Moses P G, Miao M, Yan Q and Van de Walle C G 2011 *The Journal of Chemical Physics* **134** 084703
- [50] Blöchl P E 1994 *Physical Review B* **50** 17953–17979
- [51] Kresse G and Joubert D 1999 *Physical Review B* **59** 1758–1775
- [52] Kresse G and Hafner J 1993 *Physical Review B* **48** 13115–13118
- [53] Kresse G and Furthmüller J 1996 *Physical Review B* **54** 11169–11186
- [54] Vreken Q 1968 *Journal of Physics and Chemistry of Solids* **29** 129–141
- [55] Molenkamp L W, Eppenga R, 't Hooft G W, Dawson P, Foxon C T and Moore K J 1988 *Physical Review B* **38** 4314–4317
- [56] Neumann C, Nöthe A and Lipari N O 1988 *Physical Review B* **37** 922–932
- [57] Binggeli N and Baldereschi A 1991 *Physical Review B* **43** 14734(R)
- [58] Lawaetz P 1971 *Physical Review B* **4** 3460–3467
- [59] Kim K, Lambrecht W R L, Segall B and van Schilfgaarde M 1997 *Physical Review B* **56** 7363–7375
- [60] Yeo Y C, Chong T C and Li M F 1998 *Journal of Applied Physics* **83** 1429
- [61] Rezaei B, Asgari A and Kalafi M 2006 *Physica B: Condensed Matter* **371** 107–111
- [62] Kim Y S, Marsman M, Kresse G, Tran F and Blaha P 2010 *Physical Review B* **82** 205212
- [63] Cheiwchanchamnangij T and Lambrecht W R L 2011 *Physical Review B* **84** 035203
- [64] Suzuki M, Uenoyama T and Yanase A 1995 *Physical Review B* **52** 8132–8139
- [65] Pugh S K, Dugdale D J, Brand S and Abram R A 1999 *Semiconductor Science and Technology* **14** 23–31
- [66] Ren G B, Liu Y M and Blood P 1999 *Applied Physics Letters* **74** 1117
- [67] Fritsch D, Schmidt H and Grundmann M 2003 *Physical Review B* **67** 235205
- [68] Rinke P, Winkelkemper M, Qteish A, Bimberg D, Neugebauer J and Scheffler M 2008 *Physical Review B* **77** 075202
- [69] Punya A and Lambrecht W R L 2012 *Physical Review B* **85** 195147
- [70] Cardona M and HPollak F 1966 *Physical Review* **142** 530
- [71] <http://reference.wolfram.com/applications/eda/FittingDataToNonlinearModels.html> accessed: 2015-08-21
- [72] Adams L, Nazareth J, Society A M, Statistics I M and Mathematics S 1996 *Proceedings in Applied Mathematics Series* (Society for Industrial and Applied Mathematics)
- [73] Ostromek T E 1996 *Physical Review B* **54** 14467

Supplementary Data to Stability and accuracy control of k.p parameters

Carlos M. O. Bastos,¹ Fernando P. Sabino,¹ Paulo E. Faria Junior,^{1,2}
Tiago Campos,¹ Juarez L. F. Da Silva,³ and Guilherme M. Sipahi^{1,2}

¹*São Carlos Institute of Physics, University of São Paulo,
PO Box 369, 13560-970, São Carlos, SP, Brazil.*

²*Department of Physics, State University of New York at Buffalo, 14260, Buffalo, New York, USA*

³*São Carlos Institute of Chemistry, University of São Paulo,
PO Box 780, 13560-970, São Carlos, SP, Brazil.*

I. THE k·p METHOD

The quantum-mechanical treatment of the many body problem composed by electrons and nuclei in solid state materials is a complex task, in particular, due to the electron-electron interactions. Along the years, several approaches have been proposed to address this problem, which include the solution of the Schroedinger equation using trial wave functions at different levels of approximations such as the Hartree-Fock method combined with Møller-Plesset perturbation theory or methods based on DFT [1, 2]. Although accurate, these methods are computationally demanding. The limit of thousand-atoms on one system using state-of-the-art computational resources precludes their use on mesoscopic and even in nanoscopic systems, e.g., a 100 Å wide zinc blende GaAs nanowire would demand at least 950 atoms for the correct description of one atomic layer. Plenty of interesting problems reside beyond this hard wall barrier. Alternatively, the use of the crystal symmetry to extract the main features of the electronic structure leads to another class of approaches that overcome the computational resources barrier, known generally as effective mass methods. In such methods, the many-body problem can be simplified by using an approximation in which an effective single electron moves in the field generated by the screened electron-nuclei and electron-electron systems. When many bands are included in this description the method is known as the **k·p** method, and have been used since the 50's [3–5] to predict electronic and optical properties of semiconductors.

Below, we will summarize the key features of the **k·p** method as it is described in several references elsewhere [3, 6, 7]. The one-electron Hamiltonian including relativistic SOC effects can be written as follows,

$$H = \frac{p^2}{2m_0} + V(\mathbf{r}) + \frac{\hbar}{4m_0^2c^2} [\nabla V(\mathbf{r}) \times \mathbf{p}] \cdot \boldsymbol{\sigma}, \quad (1)$$

where the first term is the kinetic energy of the electrons, the second term is the effective potential experienced by the electrons and the last term is the SOC contribution. The linear momentum operator is given by $\mathbf{p} = -i\hbar\nabla$, m_0 is the electron mass, c is the velocity of light, \hbar is the Planck constant divided by 2π and $\boldsymbol{\sigma}$ is a vector containing the Pauli matrices. Due to the translational symmetry of ideal crystalline systems, the effective potential is a periodic function, and hence, the wave function solution must satisfy the Bloch's theorem, i.e.,

$$\Psi_{n,\mathbf{k}}(\mathbf{r}) = e^{i\mathbf{k}\cdot\mathbf{r}} u_{n,\mathbf{k}}(\mathbf{r}), \quad (2)$$

where $\Psi(\mathbf{r})$ is the total wave function (known as the Bloch function), \mathbf{k} is a wave vector usually restricted to the FBZ, $u_{n,\mathbf{k}}(\mathbf{r})$ is a function with the same period as the crystal, and n indicates the energy band index. A simple algebraic manipulation shows that

$$\mathbf{p}\Psi_{n,\mathbf{k}}(\mathbf{r}) = e^{i\mathbf{k}\cdot\mathbf{r}} (\hbar\mathbf{k} + \mathbf{p})u_{n,\mathbf{k}}(\mathbf{r}), \quad (3)$$

and by applying this transformation on the wave functions (2), the Hamiltonian (1), from now on identified as H_{kp} , may be simplified to act only on the periodic functions, $u_{n,\mathbf{k}}(\mathbf{r})$, i.e.,

$$H_{kp} u_{n,\mathbf{k}}(\mathbf{r}) = E_n(\mathbf{k})u_{n,\mathbf{k}}(\mathbf{r}), \quad (4)$$

where,

$$\begin{aligned} H_{kp} = & \frac{p^2}{2m_0} + V(\mathbf{r}) + \frac{\hbar^2 k^2}{2m_0} + \frac{\hbar}{m_0} \mathbf{k} \cdot \mathbf{p} \\ & + \frac{\hbar}{4m_0^2c^2} [\nabla V(\mathbf{r}) \times \mathbf{p}] \cdot \boldsymbol{\sigma} + \frac{\hbar^2}{4m_0^2c^2} \mathbf{k} \cdot [\boldsymbol{\sigma} \times \nabla V(\mathbf{r})]. \end{aligned} \quad (5)$$

Equation (5) is the $\mathbf{k} \cdot \mathbf{p}$ Hamiltonian with SOC. This is an exact Hamiltonian that describes the motion of an electron in a periodic crystal. Despite been exact, there is no analytical solution for equation (4) and, at least, three approximations should be made in order to solve it to a certain degree.

The first approximation is to assume that we know the solutions for a particular point in reciprocal space, usually defined as k_0 . Then, we can expand Hamiltonian (5) around such point, and separate it into two different terms: one containing only non-vanishing terms at the expansion point

$$H_0 = \frac{p^2}{2m_0} + V(\mathbf{r}) + \frac{\hbar^2 k_0^2}{2m_0} + \frac{\hbar}{m_0} \mathbf{k}_0 \cdot \mathbf{p} + \frac{\hbar^2}{4m_0^2 c^2} \mathbf{k}_0 \cdot [\boldsymbol{\sigma} \times \nabla V(\mathbf{r})], \quad (6)$$

and the other containing the other terms

$$\begin{aligned} H_P = & \frac{\hbar^2}{2m_0} (k^2 - k_0^2) + \frac{\hbar}{m_0} (\mathbf{k} - \mathbf{k}_0) \cdot \mathbf{p} \\ & + \frac{\hbar}{4m_0^2 c^2} [\nabla V(\mathbf{r}) \times \mathbf{p}] \cdot \boldsymbol{\sigma} + \frac{\hbar^2}{4m_0^2 c^2} (\mathbf{k} - \mathbf{k}_0) \cdot [\boldsymbol{\sigma} \times \nabla V(\mathbf{r})]. \end{aligned} \quad (7)$$

Rewriting equation (4), we get

$$H_{kp} u_{n,\mathbf{k}}(\mathbf{r}) = (H_0 + H_P) u_{n,\mathbf{k}}(\mathbf{r}) = E_n(\mathbf{k}) u_{n,\mathbf{k}}(\mathbf{r}). \quad (8)$$

The second approximation is to define a basis set for equation (8). In principle a complete basis set would be all orbitals on each atom of the basis of the crystal structure, i. e., any state from any atom of the crystal unit cell. Although this basis set is complete, it does not help on solving the problem, it is too big. An educated guess would be to use a truncated basis set that describe the most important features of the host crystal. Group theory is used to determine the symmetry of the states.

The third approximation is to use perturbation theory in order to define the matrix elements of equation (8). A perturbative approach, proposed by Löwdin [8] in the early 50's is used to solve this problem. In this formalism, the states are separated into two classes, A and B. The states in class A will be chosen in order to address the energy bands of interest and consequently, will be the basis set of the Hamiltonian matrix. Class B will comprise the remaining bands of the system. Even if the remote bands are outside the energy range we are interested in, their interaction with states in class A can provide important additional terms to the Hamiltonian. Using Dirac notation, from now on, a total state of the system can be written as

$$|n\mathbf{k}\rangle = \sum_{\alpha} c_{\alpha n}(\mathbf{k}) |\alpha\rangle + \sum_{\beta} c_{\beta n}(\mathbf{k}) |\beta\rangle, \quad (9)$$

where $|\alpha\rangle$ and $|\beta\rangle$ are the states in class A and B, respectively. For clarity, we have $u_{n,\mathbf{k}}(\mathbf{r}) = \langle n\mathbf{k}|\mathbf{r}\rangle$, $u_{\alpha,\mathbf{k}_0}(\mathbf{r}) = \langle \alpha|\mathbf{r}\rangle$ and $u_{\beta,\mathbf{k}_0}(\mathbf{r}) = \langle \beta|\mathbf{r}\rangle$. The symmetry provided in the previous step is used in this one to reduce the work by indicating the terms that are forbidden by symmetry.

Therefore, the matrix elements of equation (8) are given by

$$\begin{aligned} \langle \alpha | H_0 + H_P | \alpha' \rangle = & E_{\alpha} (\mathbf{k} - \mathbf{k}_0) \delta_{\alpha\alpha'} + \langle \alpha | \frac{\hbar}{m_0} (\mathbf{k} - \mathbf{k}_0) \cdot \mathbf{p} | \alpha' \rangle \\ & + \langle \alpha | \frac{\hbar}{4m_0^2 c^2} [\nabla V(\mathbf{r}) \times \mathbf{p}] \cdot \boldsymbol{\sigma} | \alpha' \rangle \\ & + \sum_{\beta} \frac{\langle \alpha | \frac{\hbar}{m_0} (\mathbf{k} - \mathbf{k}_0) \cdot \mathbf{p} | \beta \rangle \langle \beta | \frac{\hbar}{m_0} (\mathbf{k} - \mathbf{k}_0) \cdot \mathbf{p} | \alpha' \rangle}{E_{\alpha} - E_{\beta}}, \end{aligned} \quad (10)$$

with

$$E_{\alpha} (\mathbf{k} - \mathbf{k}_0) = E_{\alpha}(\mathbf{k}_0) + \frac{\hbar^2}{2m_0} (k^2 - k_0^2), \quad (11)$$

where $E_{\alpha}(\mathbf{k}_0)$ is given by

$$H_0 u_{\alpha,\mathbf{k}_0}(\mathbf{r}) = E_{\alpha}(\mathbf{k}_0) u_{\alpha,\mathbf{k}_0}(\mathbf{r}). \quad (12)$$

The evaluation of the matrix elements in equation (10) is indeed a very complicated task. Looking carefully into this expression, one can see that the dipole moments (proportional to the matrix elements $\langle \alpha | \frac{\hbar}{m_0} (\mathbf{k} - \mathbf{k}_0) \cdot \mathbf{p} | \beta \rangle$) of all the transitions among the different states in the description are needed, as well as the transition energies associated with them (E_α and E_β). An alternative approach to look for all these data and performing all these sums, would be determining their functional form using group theory arguments [3, 5, 9], replacing their analytical definitions by a parametrization.

Our material of choice is the zinc blende GaAs that has a direct band gap with the maximum valence band (VBM) and the minimum conduction band (CBM) at the Γ -point. Thus, to investigate electronic properties such as optical transitions and transport, the choice of the Γ -point ($\mathbf{k}_0 = \mathbf{0}$) for the unperturbed Hamiltonian is straightforward. We considered as class A the following electronic states, the topmost six states in the valence band (VB) (usually referred to as p -like states) and the first two states at the conduction band (CB) (usually referred to as s -like states), as described below:

$$\begin{aligned} |\text{HH} \uparrow\rangle &= \frac{1}{\sqrt{2}} |(X + iY) \uparrow\rangle & |\text{HH} \downarrow\rangle &= \frac{i}{\sqrt{2}} |(X - iY) \downarrow\rangle \\ |\text{LH} \uparrow\rangle &= \frac{i}{\sqrt{6}} |(X + iY) \downarrow - 2Z \uparrow\rangle & |\text{LH} \downarrow\rangle &= \frac{1}{\sqrt{6}} |(X - iY) \uparrow + 2Z \downarrow\rangle, \\ |\text{SO} \uparrow\rangle &= \frac{1}{\sqrt{3}} |(X + iY) \downarrow + Z \uparrow\rangle & |\text{SO} \downarrow\rangle &= \frac{i}{\sqrt{3}} |-(X - iY) \uparrow + Z \downarrow\rangle \\ |\text{CB} \uparrow\rangle &= |S \uparrow\rangle & |\text{CB} \downarrow\rangle &= |S \downarrow\rangle \end{aligned} \quad (13)$$

where HH, LH and SO are the heavy hole, light hole and split-off hole valence band states, respectively, and CB is the conduction band state. \uparrow and \downarrow represent a pseudo-spin variable used to distinguish the degenerate solutions at Γ -point.

In the zinc blende symmetry group, T_d , the Bloch functions at Γ -point have the following symmetries [9, 10]: $|X\rangle \sim x$, $|Y\rangle \sim y$, $|Z\rangle \sim z$ and $|S\rangle \sim x^2 + y^2 + z^2$. The symbol \sim means that the state on the left (e. g., $|X\rangle$) transforms as the function on the right (e. g., x -coordinate) under the symmetry operations of the T_d group. The linear combinations of $|X\rangle$, $|Y\rangle$, $|Z\rangle$ and $|S\rangle$ given in the basis set (13) diagonalizes the SOC interaction at $\mathbf{k} = (0, 0, 0)$ [6, 11]. The matrix representation of (10) in the basis set (13) is

$$\begin{pmatrix} Q & S & R & 0 & i\frac{S}{\sqrt{2}} & -i\sqrt{2}R & -iP_- & 0 \\ S^\dagger & T & 0 & R & i\frac{(T-Q)}{\sqrt{2}} & i\sqrt{\frac{3}{2}}S & \sqrt{\frac{2}{3}}P_z & -\frac{1}{\sqrt{3}}P_- \\ R^\dagger & 0 & T & -S & -i\sqrt{\frac{3}{2}}S^\dagger & i\frac{(T-Q)}{\sqrt{2}} & -\frac{i}{\sqrt{3}}P_+ & -i\sqrt{\frac{2}{3}}P_z \\ 0 & R^\dagger & -S^\dagger & Q & -i\sqrt{2}R^\dagger & -i\frac{S^\dagger}{\sqrt{2}} & 0 & -P_+ \\ -i\frac{S^\dagger}{\sqrt{2}} & -i\frac{(T-Q)^\dagger}{\sqrt{2}} & i\sqrt{\frac{3}{2}}S & i\sqrt{2}R & \frac{Q+T}{2} + \Delta_{so} & 0 & -\frac{i}{\sqrt{3}}P_z & -i\sqrt{\frac{2}{3}}P_- \\ i\sqrt{2}R^\dagger & -i\sqrt{\frac{3}{2}}S^\dagger & -i\frac{(T-Q)^\dagger}{\sqrt{2}} & i\frac{S}{\sqrt{2}} & 0 & \frac{Q+T}{2} + \Delta_{so} & \sqrt{\frac{2}{3}}P_+ & -\frac{1}{\sqrt{3}}P_z \\ -iP_- & \sqrt{\frac{2}{3}}P_z & \frac{i}{\sqrt{3}}P_- & 0 & \frac{i}{\sqrt{3}}P_z & \sqrt{\frac{2}{3}}P_- & E_c & 0 \\ 0 & -\frac{1}{\sqrt{3}}P_+ & i\sqrt{\frac{2}{3}}P_z & -P_- & i\sqrt{\frac{2}{3}}P_+ & -\frac{1}{\sqrt{3}}P_z & 0 & E_c \end{pmatrix} \quad (14)$$

where the terms are given by

$$\begin{aligned} Q &= -\frac{\hbar^2}{2m_0} [(\tilde{\gamma}_1 + \tilde{\gamma}_2)(k_x^2 + k_y^2) - (\tilde{\gamma}_1 - 2\tilde{\gamma}_2)k_z^2] & R &= -\frac{\hbar^2}{2m_0}\sqrt{3} [\tilde{\gamma}_2(k_x^2 - k_y^2) + 2i\tilde{\gamma}_3k_xk_y] \\ E_c &= E_g + \frac{\hbar^2}{2m_0}\tilde{\epsilon}k^2 & P_z &= Pk_z \\ T &= -\frac{\hbar^2}{2m_0} [(\tilde{\gamma}_1 - \tilde{\gamma}_2)(k_x^2 + k_y^2) + (\tilde{\gamma}_1 + 2\tilde{\gamma}_2)k_z^2] & S &= i\frac{\hbar^2}{2m_0} [2\sqrt{3}\tilde{\gamma}_3k_z(k_x - ik_y)] \\ P_\pm &= \frac{1}{\sqrt{2}}P(k_x \pm ik_y) & k^2 &= k_x^2 + k_y^2 + k_z^2 \end{aligned} \quad (15)$$

II. ANALYTICAL FUNCTIONS FOR THE Γ -K AND Γ -L DIRECTIONS

In the main article, we presented the general procedure to determine analytical functions and their numerical counterparts. In this appendix we show the functions for all directions used in this work.

For the Γ - X direction:

$$\begin{aligned}
c_{HH}^A(k_{\Gamma X}, \{p\}) &= -(\tilde{\gamma}_1 - 2\tilde{\gamma}_2) \frac{\hbar^2 k_{\Gamma X}^2}{2m_0} \\
c_0^A(k_{\Gamma X}, \{p\}) &= \Delta_{so} - E_g + [2(\tilde{\gamma}_1 + \tilde{\gamma}_2) - \tilde{e}] \frac{\hbar^2 k_{\Gamma X}^2}{2m_0} \\
c_1^A(k_{\Gamma X}, \{p\}) &= -\Delta_{so} E_g - \left[\Delta_{so} (\tilde{e} - \tilde{\gamma}_1 - 2\tilde{\gamma}_2) + 2E_g (\tilde{\gamma}_1 + \tilde{\gamma}_2) + \frac{2m_0}{\hbar^2} P^2 \right] \frac{\hbar^2 k_{\Gamma X}^2}{2m_0} \\
&\quad + [-2\tilde{e}(\tilde{\gamma}_1 + \tilde{\gamma}_2) + \tilde{\gamma}_1^2 + 2\tilde{\gamma}_1 \tilde{\gamma}_2 - 8\tilde{\gamma}_2^2] \left(\frac{\hbar^2 k_{\Gamma X}^2}{2m_0} \right)^2 \\
c_2^A(k_{\Gamma X}, \{p\}) &= - \left[\Delta_{so} E_g (\tilde{\gamma}_1 + 2\tilde{\gamma}_2) + \frac{2}{3} \Delta_{so} \frac{2m_0}{\hbar^2} P^2 \right] \frac{\hbar^2}{2m_0} k_{\Gamma X}^2 \\
&\quad - \left[\Delta_{so} \tilde{e} (\tilde{\gamma}_1 + 2\tilde{\gamma}_2) + E_g (\tilde{\gamma}_1 + 4\tilde{\gamma}_2) (\tilde{\gamma}_1 - 2\tilde{\gamma}_2) + \frac{2m_0}{\hbar^2} P^2 (\tilde{\gamma}_1 - 2\tilde{\gamma}_2) \right] \left(\frac{\hbar^2 k_{\Gamma X}^2}{2m_0} \right)^2 \\
&\quad - \tilde{e} (\tilde{\gamma}_1 + 4\tilde{\gamma}_2) (\tilde{\gamma}_1 - 2\tilde{\gamma}_2) \left(\frac{\hbar^2 k_{\Gamma X}^2}{2m_0} \right)^3
\end{aligned} \tag{16}$$

where $k_{\Gamma X}$ indicates a point along the $\Gamma - X$ direction. Please notice that in these expressions the Kane parameter P appear always as part of its energetic counterpart $E_P = 2m_0 P^2 / \hbar^2$.

For the Γ - K direction we have

$$\begin{aligned}
c_0^A(k_{\Gamma K}, \{p\}) &= \Delta_{so} - E_g - (\tilde{e} - 3\tilde{\gamma}_1) \frac{\hbar^2 k_{\Gamma K}^2}{2m_0} \\
c_1^A(k_{\Gamma K}, \{p\}) &= -\Delta_{so} E_g - \left[\Delta_{so} (\tilde{e} - 2\tilde{\gamma}_1) + 3E_g \tilde{\gamma}_1 + \frac{2m_0}{\hbar^2} P^2 \right] \frac{\hbar^2 k_{\Gamma K}^2}{2m_0} \\
&\quad - [3\tilde{e}\tilde{\gamma}_1 - 3\tilde{\gamma}_1^2 + 3\tilde{\gamma}_2^2 + 9\tilde{\gamma}_3^2] \left(\frac{\hbar^2 k_{\Gamma K}^2}{2m_0} \right)^2 \\
c_2^A(k_{\Gamma K}, \{p\}) &= - \left[2\Delta_{so} E_g \tilde{\gamma}_1 + \frac{2}{3} \Delta_{so} \frac{2m_0}{\hbar^2} P^2 \right] \frac{\hbar^2 k_{\Gamma K}^2}{2m_0} \\
&\quad - [2(\tilde{e}\tilde{\gamma}_1 - \tilde{\gamma}_1^2 + \tilde{\gamma}_2^2 + 3\tilde{\gamma}_3^2) \Delta_{so} - 3(-\tilde{\gamma}_1^2 + \tilde{\gamma}_2^2 + \tilde{\gamma}_3^2) E_g \\
&\quad + (2\tilde{\gamma}_1 - \tilde{\gamma}_2 - 3\tilde{\gamma}_3) \frac{2m_0}{\hbar^2} P^2] \left(\frac{\hbar^2 k_{\Gamma K}^2}{2m_0} \right)^2 \\
&\quad - [3\tilde{e}(\tilde{\gamma}_1^2 - \tilde{\gamma}_2^2 - 3\tilde{\gamma}_3^2) + \tilde{\gamma}_1(-\tilde{\gamma}_1^2 + 3\tilde{\gamma}_2^2 + 9\tilde{\gamma}_3^2) + 2\tilde{\gamma}_2^3 - 18\tilde{\gamma}_2\tilde{\gamma}_3^2] \left(\frac{\hbar^2 k_{\Gamma K}^2}{2m_0} \right)^3 \\
c_3^A(k_{\Gamma K}, \{p\}) &= - \left[\Delta_{so} E_g (\tilde{\gamma}_1^2 - \tilde{\gamma}_2^2 - 3\tilde{\gamma}_3^2) + \frac{\Delta_{so}}{3} (2\tilde{\gamma}_1 - \tilde{\gamma}_2 - 3\tilde{\gamma}_3) \frac{2m_0}{\hbar^2} P^2 \right] \left(\frac{\hbar^2 k_{\Gamma K}^2}{2m_0} \right)^2 \\
&\quad - [\Delta_{so} \tilde{e} (\tilde{\gamma}_1^2 - \tilde{\gamma}_2^2 - 3\tilde{\gamma}_3^2) + E_g (\tilde{\gamma}_1 - 2\tilde{\gamma}_2) (\tilde{\gamma}_1 + \tilde{\gamma}_2 + 3\tilde{\gamma}_3) (\tilde{\gamma}_1 + \tilde{\gamma}_2 - 3\tilde{\gamma}_3) \\
&\quad + (\tilde{\gamma}_1 - 2\tilde{\gamma}_2) (\tilde{\gamma}_1 + \tilde{\gamma}_2 - 3\tilde{\gamma}_3) \frac{2m_0}{\hbar^2} P^2] \left(\frac{\hbar^2 k_{\Gamma K}^2}{2m_0} \right)^3 \\
&\quad - \tilde{e} (\tilde{\gamma}_1 - 2\tilde{\gamma}_2) (\tilde{\gamma}_1 + \tilde{\gamma}_2 + 3\tilde{\gamma}_3) (\tilde{\gamma}_1 + \tilde{\gamma}_2 - 3\tilde{\gamma}_3) \left(\frac{\hbar^2 k_{\Gamma K}^2}{2m_0} \right)^4
\end{aligned} \tag{17}$$

with the numerical counterpart being

$$\begin{aligned}
c_0^N(k_{\Gamma K}) &= -\epsilon_{CB}(k_{\Gamma K}) - \epsilon_{LH}(k_{\Gamma K}) - \epsilon_{SO}(k_{\Gamma K}) - \epsilon_{HH}(k_{\Gamma K}) \\
c_1^N(k_{\Gamma K}) &= \epsilon_{CB}(k_{\Gamma K})\epsilon_{LH}(k_{\Gamma K}) + \epsilon_{SO}(k_{\Gamma K})\epsilon_{LH}(k_{\Gamma K}) + \epsilon_{HH}(k_{\Gamma K})\epsilon_{LH}(k_{\Gamma K}) + \epsilon_{CB}(k_{\Gamma K})\epsilon_{SO}(k_{\Gamma K}) + \\
&\quad \epsilon_{CB}(k_{\Gamma K})\epsilon_{HH}(k_{\Gamma K}) + \epsilon_{SO}(k_{\Gamma K})\epsilon_{HH}(k_{\Gamma K}) \\
c_2^N(k_{\Gamma K}) &= -\epsilon_{CB}(k_{\Gamma K})\epsilon_{LH}(k_{\Gamma K})\epsilon_{SO}(k_{\Gamma K}) - \epsilon_{CB}(k_{\Gamma K})\epsilon_{HH}(k_{\Gamma K})\epsilon_{SO}(k_{\Gamma K}) - \epsilon_{LH}(k_{\Gamma K})\epsilon_{HH}(k_{\Gamma K})\epsilon_{SO}(k_{\Gamma K}) - \\
&\quad \epsilon_{CB}(k_{\Gamma K})\epsilon_{LH}(k_{\Gamma K})\epsilon_{HH}(k_{\Gamma K}) \\
c_3^N(k_{\Gamma K}) &= \epsilon_{CB}(k_{\Gamma K})\epsilon_{LH}(k_{\Gamma K})\epsilon_{SO}(k_{\Gamma K})\epsilon_{HH}(k_{\Gamma K})
\end{aligned} \tag{18}$$

The Γ - L direction functions are

$$\begin{aligned}
c_{HH}^A(k_{\Gamma L}, \{p\}) &= -(\tilde{\gamma}_1 - 2\tilde{\gamma}_3) \frac{\hbar^2 k_{\Gamma L}^2}{2m_0} \\
c_0^A(k_{\Gamma L}, \{p\}) &= \Delta_{SO} - E_g + [2(\tilde{\gamma}_1 + \tilde{\gamma}_3) - \tilde{e}] \frac{\hbar^2 k_{\Gamma L}^2}{2m_0} \\
c_1^A(k_{\Gamma L}, \{p\}) &= -\Delta_{SO} E_g - \left[\Delta_{SO}(\tilde{e} - \tilde{\gamma}_1 - 2\tilde{\gamma}_3) + 2E_g(\tilde{\gamma}_1 + \tilde{\gamma}_3) + \frac{2m_0}{\hbar^2} P^2 \right] \frac{\hbar^2 k_{\Gamma L}^2}{2m_0} \\
&\quad + [-2\tilde{e}(\tilde{\gamma}_1 + \tilde{\gamma}_3) + \tilde{\gamma}_1^2 + 2\tilde{\gamma}_1\tilde{\gamma}_3 - 8\tilde{\gamma}_3^2] \left(\frac{\hbar^2 k_{\Gamma L}^2}{2m_0} \right)^2 \\
c_2^A(k_{\Gamma L}, \{p\}) &= -\left[\Delta_{SO} E_g(\tilde{\gamma}_1 + 2\tilde{\gamma}_3) + \frac{2}{3} \Delta_{SO} \frac{2m_0}{\hbar^2} P^2 \right] \frac{\hbar^2 k_{\Gamma L}^2}{2m_0} \\
&\quad - \left[\Delta_{SO} \tilde{e}(\tilde{\gamma}_1 + 2\tilde{\gamma}_3) + E_g(\tilde{\gamma}_1 + 4\tilde{\gamma}_3)(\tilde{\gamma}_1 - 2\tilde{\gamma}_3) + \frac{2m_0}{\hbar^2} P^2(\tilde{\gamma}_1 - 2\tilde{\gamma}_3) \right] \left(\frac{\hbar^2 k_{\Gamma L}^2}{2m_0} \right)^2 \\
&\quad - \tilde{e}(\tilde{\gamma}_1 + 4\tilde{\gamma}_3)(\tilde{\gamma}_1 - 2\tilde{\gamma}_3) \left(\frac{\hbar^2 k_{\Gamma L}^2}{2m_0} \right)^3
\end{aligned} \tag{19}$$

and their numerical counterpart

$$\begin{aligned}
c_{HH}^N(k_{\Gamma L}) &= -\epsilon_{HH}(k_{\Gamma L}) \\
c_0^N(k_{\Gamma L}) &= -\epsilon_{CB}(k_{\Gamma L}) - \epsilon_{LH}(k_{\Gamma L}) - \epsilon_{SO}(k_{\Gamma L}) \\
c_1^N(k_{\Gamma L}) &= \epsilon_{CB}(k_{\Gamma L})\epsilon_{LH}(k_{\Gamma L}) + \epsilon_{SO}(k_{\Gamma L})\epsilon_{LH}(k_{\Gamma L}) + \epsilon_{CB}(k_{\Gamma L})\epsilon_{SO}(k_{\Gamma L}) \\
c_2^N(k_{\Gamma L}) &= -\epsilon_{CB}(k_{\Gamma L})\epsilon_{LH}(k_{\Gamma L})\epsilon_{SO}(k_{\Gamma L})
\end{aligned} \tag{20}$$

III. 6X6 HAMILTONIAN

In the paper, we considered the 8×8 Kane Hamiltonian. However, for large gap materials or when the interest relies in effects occurring only inside the valence band, we can neglect the interaction between the conduction and valence bands, setting the parameter P to zero. In such approach, we can define two independent A classes, one for valence band (2×2) states and the other for the conduction band states (6×6), obtaining a new Hamiltonian that will be denoted as 6×6 [7].

Although the functional form of the 6×6 and 8×8 terms are the same, the different choices for the A classes requires

correction in the effective mass parameters. The Hamiltonian is given by the following matrix

$$\begin{pmatrix} Q & S & R & 0 & i\frac{S}{\sqrt{2}} & -i\sqrt{2}R & 0 & 0 \\ S^\dagger & T & 0 & R & i\frac{(T-Q)}{\sqrt{2}} & i\sqrt{\frac{3}{2}}S & 0 & 0 \\ R^\dagger & 0 & T & -S & -i\sqrt{\frac{3}{2}}S^\dagger & i\frac{(T-Q)}{\sqrt{2}} & 0 & 0 \\ 0 & R^\dagger & -S^\dagger & Q & -i\sqrt{2}R^\dagger & -i\frac{S^\dagger}{\sqrt{2}} & 0 & 0 \\ -i\frac{S^\dagger}{\sqrt{2}} & -i\frac{(T-Q)^\dagger}{\sqrt{2}} & i\sqrt{\frac{3}{2}}S & i\sqrt{2}R & \frac{Q+T}{2} + \Delta_{so} & 0 & 0 & 0 \\ i\sqrt{2}R^\dagger & -i\sqrt{\frac{3}{2}}S^\dagger & -i\frac{(T-Q)^\dagger}{\sqrt{2}} & i\frac{S}{\sqrt{2}} & 0 & \frac{Q+T}{2} + \Delta_{so} & 0 & 0 \\ 0 & 0 & 0 & 0 & 0 & 0 & E_c & 0 \\ 0 & 0 & 0 & 0 & 0 & 0 & 0 & E_c \end{pmatrix} \quad (21)$$

with the terms being

$$\begin{aligned} Q &= -\frac{\hbar^2}{2m_0} [(\gamma_1 + \gamma_2)(k_x^2 + k_y^2) - (\gamma_1 - 2\gamma_2)k_z^2] & T &= \frac{\hbar^2}{2m_0} [(\gamma_2 - \gamma_1)(k_x^2 + k_y^2) - (\gamma_1 + 2\gamma_2)k_z^2] \\ R &= \frac{\hbar^2}{2m_0} \sqrt{3} [(2i\gamma_3 k_x k_y) + \gamma_2(k_x^2 - k_y^2)] & S &= \frac{\hbar^2}{2m_0} [2\sqrt{3}i\gamma_3 k_z(k_x - ik_y)] \\ E_c &= E_g + e\frac{\hbar^2 k^2}{2m_0} & k^2 &= k_x^2 + k_y^2 + k_z^2. \end{aligned} \quad (22)$$

IV. FITTING FUNCTIONS OF THE 6X6 HAMILTONIAN

We also applied the fitting method to obtain the parameters for the 6×6 Hamiltonian (21) as described in section 3 in the paper. In this Hamiltonian, valence and conduction band are decoupled and can be treated independently. As conduction band is a diagonal block with dimension 2, we have the following polynomial equation:

$$[-\epsilon + c_0^A(\mathbf{k}, \{p\})]^2 = 0, \quad (23)$$

where the square in the expression means a the two-fold degeneracy of the eigenvalues. The analytical coefficient is then given by

$$c_0^A(\mathbf{k}, \{p\}) = E_g + e\frac{\hbar^2 k^2}{2m_0}, \quad (24)$$

and the parameter set, $\{p\}$, in this case, is $\{e, E_g\}$.

e is determined through the fitting of the conduction band to a parabolic curve (24) and E_g is extracted from the DFT-HSE band structure. For the valence band, also two-fold degenerated, we have the following secular equation

$$[\epsilon^3 + c_2^N(\mathbf{k}, \{p\})\epsilon^2 + c_1^N(\mathbf{k}, \{p\})\epsilon + c_0^N(\mathbf{k}, \{p\})]^2 = 0, \quad (25)$$

with the parameter set being $\{p\} = \{\gamma_1, \gamma_2, \gamma_3, \Delta_{so}\}$.

The sampling directions were chosen to be the same used in the 8×8 model, i. e., $\Gamma - X$, $\Gamma - K$ and $\Gamma - L$. The analytical coefficients for the $\Gamma - X$ direction are

$$\begin{aligned} c_{HH}^A(k_{\Gamma X}, \{p\}) &= -[\gamma_1 - 2\gamma_2] \frac{\hbar^2 k_{\Gamma X}^2}{2m_0} \\ c_0^A(k_{\Gamma X}, \{p\}) &= \Delta_{so} + 2[\gamma_1 + \gamma_2] \frac{\hbar^2 k_{\Gamma X}^2}{2m_0} \\ c_1^A(k_{\Gamma X}, \{p\}) &= \Delta_{so} [\gamma_1 + 2\gamma_2] \frac{\hbar^2 k_{\Gamma X}^2}{2m_0} + [\gamma_1^2 + 2\gamma_1\gamma_2 - 8\gamma_2^2] \left(\frac{k_{\Gamma X}^2}{2m_0} \right)^2 \end{aligned} \quad (26)$$

and the numerical coefficients

$$\begin{aligned} c_{HH}^N(k_{\Gamma X}) &= \epsilon_{HH}(k_{\Gamma X}) \\ c_1^N(k_{\Gamma X}) &= -\epsilon_{LH}(k_{\Gamma X}) - \epsilon_{SO}(k_{\Gamma X}) \\ c_0^N(k_{\Gamma X}) &= \epsilon_{LH}(k_{\Gamma X})\epsilon_{SO}(k_{\Gamma X}). \end{aligned} \quad (27)$$

For the $\Gamma - K$ direction we have

$$\begin{aligned}
c_0^A(k_{\Gamma K}, \{p\}) &= \Delta_{so} + 3\gamma_1 \frac{\hbar^2 k_{\Gamma K}^2}{2m_0} \\
c_1^A(k_{\Gamma K}, \{p\}) &= 2\Delta_{so}\gamma_1 \frac{\hbar^2 k_{\Gamma K}^2}{2m_0} + 3[\gamma_1^2 - \gamma_2^2 - 3\gamma_3^2] \left(\frac{\hbar^2 k_{\Gamma K}^2}{2m_0} \right)^2 \\
c_2^A(k_{\Gamma K}, \{p\}) &= \Delta_{so} [\gamma_1^2 - \gamma_2^2 - 3\gamma_3^2] \left(\frac{\hbar^2 k_{\Gamma K}^2}{2m_0} \right)^2 + (\gamma_1 - 2\gamma_2) [\gamma_1^2 + 2\gamma_1\gamma_2 + \gamma_2^2 - 9\gamma_3^2] \left(\frac{\hbar^2 k_{\Gamma K}^2}{2m_0} \right)^3
\end{aligned} \tag{28}$$

with the numerical coefficients

$$\begin{aligned}
c_2^N(k_{\Gamma K}) &= -\epsilon_{HH}(k_{\Gamma K}) - \epsilon_{LH}(k_{\Gamma K}) - \epsilon_{SO}(k_{\Gamma K}) \\
c_1^N(k_{\Gamma K}) &= \epsilon_{HH}(k_{\Gamma K})\epsilon_{LH}(k_{\Gamma K}) + \epsilon_{HH}(k_{\Gamma K})\epsilon_{SO}(k_{\Gamma K}) + \epsilon_{LH}(k_{\Gamma K})\epsilon_{SO}(k_{\Gamma K}) \\
c_0^N(k_{\Gamma K}) &= \epsilon_{HH}(k_{\Gamma K})\epsilon_{LH}(k_{\Gamma K})\epsilon_{SO}(k_{\Gamma K}) .
\end{aligned} \tag{29}$$

And for the $\Gamma - L$ direction we have

$$\begin{aligned}
c_{HH}^A(k_{\Gamma L}, \{p\}) &= -[\gamma_1 - 2\gamma_3] \frac{\hbar^2 k_{\Gamma L}^2}{2m_0} \\
c_0^A(k_{\Gamma L}, \{p\}) &= \Delta_{so} + 2[\gamma_1 + \gamma_3] \frac{\hbar^2 k_{\Gamma L}^2}{2m_0} \\
c_1^A(k_{\Gamma L}, \{p\}) &= \Delta_{so} [\gamma_1 + 2\gamma_3] \frac{\hbar^2 k_{\Gamma L}^2}{2m_0} + [\gamma_1^2 + 2\gamma_1\gamma_3 - 8\gamma_3^2] \left(\frac{k_{\Gamma L}^2}{2m_0} \right)^2
\end{aligned} \tag{30}$$

with the numerical coefficients

$$\begin{aligned}
c_{HH}^N(k_{\Gamma L}) &= \epsilon_{HH}(k_{\Gamma L}) \\
c_1^N(k_{\Gamma L}) &= -\epsilon_{LH}(k_{\Gamma L}) - \epsilon_{SO}(k_{\Gamma L}) \\
c_0^N(k_{\Gamma L}) &= \epsilon_{LH}(k_{\Gamma L})\epsilon_{SO}(k_{\Gamma L}) .
\end{aligned} \tag{31}$$

V. PARAMETER SETS FOR THE 6X6 HAMILTONIAN

Using the same procedure as for the 8×8 case, we performed the fitting for different regions around the Γ point obtaining a different set of parameters for each one of them. The definition of the best set of parameters was done using the RMSD analysis. Fig. V shows the values of RMSD for each different region enclosing the Γ point.

As expected, the lower RMSD values were obtained for fitting regions below 8%, where the band structure is almost parabolic. However, even for fitting regions beyond this limit, up to 12% of the FBZ, the RMSD values are still considerably small, indicating that the model can still be used.

An animated figure showing the comparison of the $\mathbf{k} \cdot \mathbf{p}$ fitting and the original DFT-HSE band structures is available with this text at <http://magazine.site>. In this animation we vary the parameters showing emphasizing the fitting region used for their extraction.

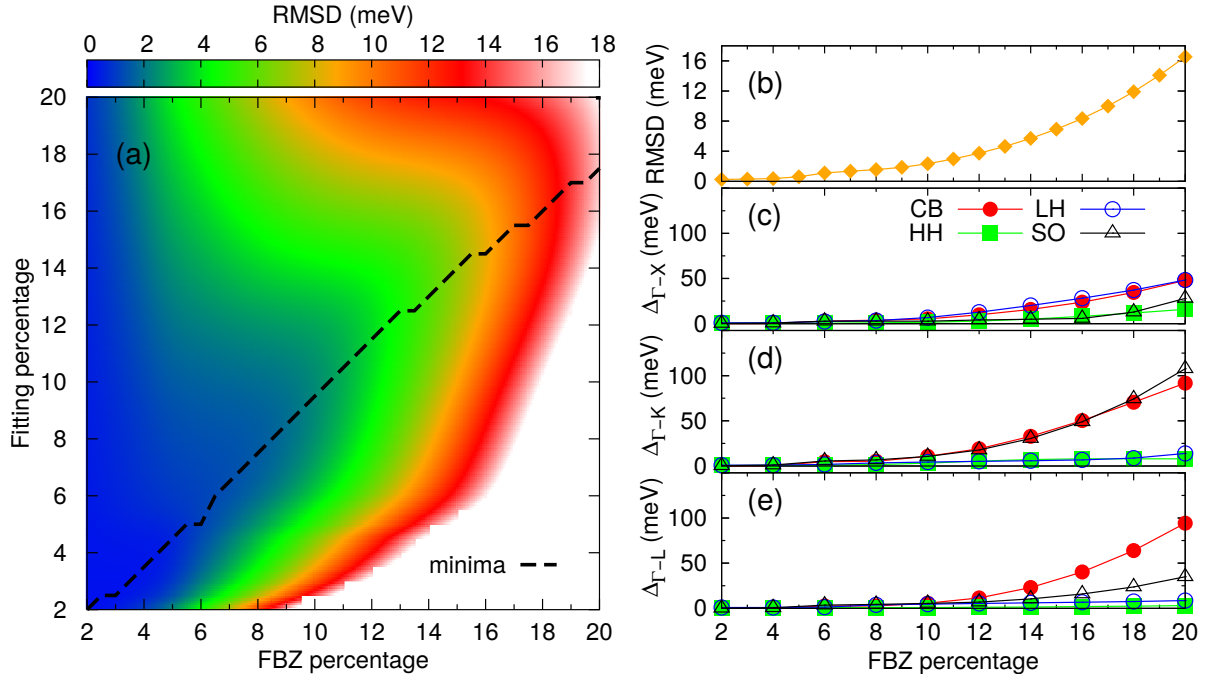


FIG. 1: (a) Root mean square deviation (RMSD) values intensity map showing the agreement of the different adjusted parameter sets against the range around the Γ -point. A dashed curve indicate the optimal parameters for each enclosed region. (b) RMSD of the optimal set of parameters for each region. (c), (d) and (e) show the maximum deviation for each optimal parameter set for the three directions.

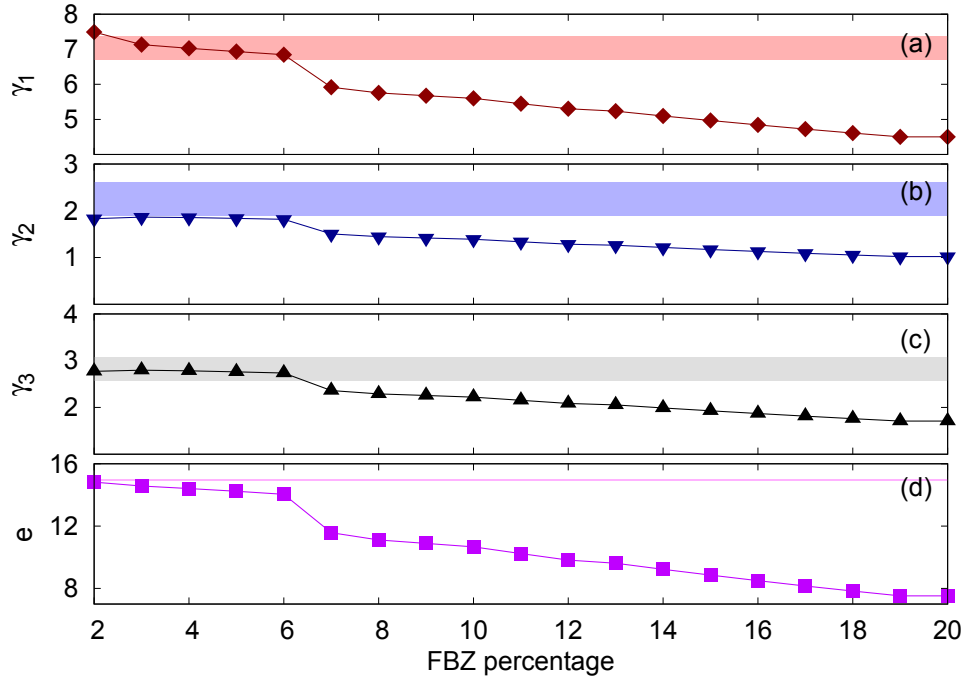


FIG. 2: Comparison of the optimal parameters with the literature. The optimal parameters are shown in the curves and the shadowed regions present the intervals of the standard deviation around the average values of the parameters, determined from 7 traditional papers [12–18] (see Table I). (a) γ_1 , (b) γ_2 , (c) γ_3 and (d) e .

Figure 2 shows the comparison of the optimal parameters with literature values. The colored regions indicate the region of one standard deviation around the average calculated with Refs. [12–18]. For small percentage of the band (up to 8%), the variation of the parameters is flat and similar the literature, i.e., for the unique set parameters

we describing this region. However, above to 8% (outside of the validity of the Hamiltonian), the parameters have variation because the developed method return the best values to describe effects non-present in the Hamiltonian.

TABLE I: Experimental data used to compute the average and standard deviation of literature parameters

	ref.[12]	ref.[13]	ref. [14]	ref. [15]	ref.[16]	ref. [17]	ref. [18]
γ_1	6.98	6.85	7.65	6.67	7.20	6.79	7.17
γ_2	2.06	2.16	2.41	1.87	2.50	1.92	2.88
γ_3	2.93	2.79	3.28	2.67	2.50	2.68	2.91
e	14.93	14.93	14.93	14.93	14.93	15.04	15.04

VI. PARAMETERS FOR REGIONS DEFINED BY DIFFERENT PERCENTAGES OF THE FBZ

TABLE II: Optimal parameter sets for different enclosing regions of the FBZ, for both Hamiltonians (6×6 and 8×8).

%	6×6 Hamiltonian					8×8 Hamiltonian				
	γ_1	γ_2	γ_3	e		$\tilde{\gamma}_1$	$\tilde{\gamma}_2$	$\tilde{\gamma}_3$	\tilde{e}	P
2	7.49	1.83	2.77	14.82		-1.26	-2.55	-1.55	-11.29	12.74
3	7.13	1.86	2.80	14.57		-0.43	-2.00	-1.02	-8.30	11.99
4	7.03	1.85	2.78	14.41		0.27	-1.55	-0.59	-5.80	11.32
5	6.93	1.84	2.76	14.24		0.64	-1.32	-0.37	-4.52	10.95
6	6.85	1.82	2.74	14.04		0.89	-1.15	-0.21	-3.68	10.69
7	5.92	1.50	2.36	11.57		1.32	-0.92	0.01	-2.33	10.22
8	5.76	1.45	2.29	11.12		1.34	-0.90	0.02	-2.22	10.16
9	5.67	1.42	2.26	10.89		1.35	-0.88	0.02	-2.19	10.12
10	5.60	1.39	2.22	10.67		1.35	-0.87	0.03	-2.17	10.09
11	5.45	1.34	2.15	10.24		1.35	-0.85	0.03	-2.17	10.06
12	5.30	1.29	2.09	9.82		1.34	-0.83	0.03	-2.18	10.03
13	5.23	1.26	2.05	9.62		1.33	-0.82	0.03	-2.19	10.00
14	5.10	1.22	1.99	9.23		1.32	-0.81	0.03	-2.20	9.99
15	4.97	1.17	1.93	8.86		1.31	-0.79	0.03	-2.22	9.96
16	4.84	1.13	1.87	8.50		1.31	-0.78	0.03	-2.24	9.94
17	4.73	1.09	1.81	8.16		1.21	-0.77	0.03	-2.27	9.91
18	4.61	1.05	1.76	7.83		1.29	-0.76	0.03	-2.29	9.90
19	4.50	1.02	1.71	7.52		1.28	-0.74	0.03	-2.32	9.86
20	4.50	1.02	1.71	7.52		1.28	-0.73	0.03	-2.34	9.85

-
- [1] P. Hohenberg, W. Kohn, Inhomogeneous Electron Gas, Physical Review 136 (3B) (1964) B864–B871.
 - [2] W. Kohn, L. J. Sham, Self-Consistent Equations Including Exchange and Correlation Effects, Physical Review 140 (4A) (1965) A1133–A1138.
 - [3] E. Kane, The k-p method, in: R. Willardson, A. C. Beer (Eds.), Semiconductors and Semimetals, Vol. 1 of Semiconductors and Semimetals, Elsevier, 1966, pp. 75 – 100.
 - [4] J. M. Luttinger, W. Kohn, Motion of Electrons and Holes in Perturbed Periodic Fields, Physical Review 97 (4) (1955) 869–883.
 - [5] G. Dresselhaus, Spin-orbit coupling effects in zinc blende structures, Physical Review 100 (2) (1955) 580–586.
 - [6] R. Enderlein, J. M. N. Horing, Fundamentals Of Semiconductor Physics And Devices, World Scientific, Singapore, 1997.
 - [7] M. Willatzen, L. C. Lew Yan Voon, The k p Method, Springer Berlin Heidelberg, Berlin, Heidelberg, 2009.
 - [8] P.-O. Löwdin, A note on the quantum-mechanical perturbation theory, The Journal of Chemical Physics 19 (11) (1951) 1396.
 - [9] M. S. Dresselhaus, G. Dresselhaus, A. Jório, Group Theory - Applications to the Physics of Condensed Matter, 1st Edition, Springer Science & Business Media, 2007.
 - [10] P. Y. Yu, M. Cardona, Fundamentals of semiconductors, Springer-Verlag, Berlin, Heidelberg, 2005.
 - [11] E. O. Kane, Band structure of indium antimonide, Journal of Physics and Chemistry of Solids 1 (4) (1957) 249–261.

- [12] I. Vurgaftman, J. R. Meyer, L. R. Ram-Mohan, Band parameters for III-V compound semiconductors and their alloys, *Journal of Applied Physics* 89 (11) (2001) 5815.
- [13] S. Shokhovets, O. Ambacher, G. Gobsch, Conduction-band dispersion relation and electron effective mass in III-V and II-VI zinc-blende semiconductors, *Physical Review B* 76 (12) (2007) 125203.
- [14] P. Lawaetz, Valence-Band Parameters in Cubic Semiconductors, *Physical Review B* 4 (10) (1971) 3460–3467.
- [15] T. Ostromek, Evaluation of matrix elements of the 8×8 k.p Hamiltonian with k-dependent spin-orbit contributions for the zinc-blende structure of GaAs, *Physical Review B* 54 (20).
- [16] Q. Vrehen, Interband magneto-optical absorption in gallium arsenide, *Journal of Physics and Chemistry of Solids* 29 (1) (1968) 129–141.
- [17] L. W. Molenkamp, R. Eppenga, G. W. 't Hooft, P. Dawson, C. T. Foxon, K. J. Moore, Determination of valence-band effective-mass anisotropy in GaAs quantum wells by optical spectroscopy, *Physical Review B* 38 (6) (1988) 4314–4317.
- [18] C. Neumann, A. Nöthe, N. O. Lipari, Two-photon magnetoabsorption of ZnTe, CdTe, and GaAs, *Physical Review B* 37 (2) (1988) 922–932.